J. Fluid Mech. (2010), *vol.* 654, *pp.* 35–63. © Cambridge University Press 2010
doi:10.1017/S0022112009993272

Balanced and unbalanced routes to dissipation in an equilibrated Eady flow

M. JEROEN MOLEMAKER[1]†, JAMES C. MCWILLIAMS[1] AND XAVIER CAPET[2]

[1]IGPP, UCLA, 405 Hilgard Avenue, Los Angeles, CA 90066, USA
[2]Laboratoire de Physique des Océans, IFREMER/CNRS, Brest, France

(Received 9 May 2007; revised 3 November 2009; accepted 5 November 2009)

The oceanic general circulation is forced at large scales and is unstable to mesoscale eddies. Large-scale currents and eddy flows are approximately in geostrophic balance. Geostrophic dynamics is characterized by an inverse energy cascade except for dissipation near the boundaries. In this paper, we confront the dilemma of how the general circulation may achieve dynamical equilibrium in the presence of continuous large-scale forcing and the absence of boundary dissipation. We do this with a forced horizontal flow with spatially uniform rotation, vertical stratification and vertical shear in a horizontally periodic domain, i.e. a version of Eady's flow carried to turbulent equilibrium. A direct route to interior dissipation is presented that is essentially non-geostrophic in its dynamics, with significant submesoscale frontogenesis, frontal instability and breakdown, and forward kinetic energy cascade to dissipation. To support this conclusion, a series of simulations is made with both quasigeostrophic and Boussinesq models. The quasigeostrophic model is shown as increasingly inefficient in achieving equilibration through viscous dissipation at increasingly higher numerical resolution (hence Reynolds number), whereas the non-geostrophic Boussinesq model equilibrates with only weak dependence on resolution and Rossby number.

Key words: geostrophic turbulence, mixing and dispersion, ocean processes

1. Introduction

The general circulations of the atmosphere and ocean are forced at large scales, and to achieve equilibrium they must viscously dissipate much of their kinetic energy at small scales. The prevailing dynamical paradigm for large and mesoscale flows includes diagnostic force-balance constraints, i.e. hydrostatic and either geostrophic or some form of gradient-wind balances (McWilliams 2003). A related paradigm is the inverse energy cascade of geostrophic turbulence (Charney 1971). Together these imply a potential dilemma for energy equilibration (Muller, McWilliams & Molemaker 2005): if the directly forced large-scale flow loses its energy by instability to balanced mesoscale eddies, then how is the eddy energy viscously dissipated if it is transferred only towards larger scales? Part of the dissipation can occur in the top or bottom turbulent boundary layers, but unless energy flux from the interior to the boundary is efficient enough, this route may not suffice. In this paper, we examine the possibility of a direct route to dissipation in the interior by a forward energy cascade involving a spontaneous violation of the diagnostic force-balance constraints.

† Email address for correspondence: nmolem@atmos.ucla.edu

We pose the highly idealized problem of an equilibrium Eady flow with a restoring forcing towards a uniformly stratified, uniform vertical shear flow in a uniformly rotating environment. This is the baroclinic flow configuration with perhaps the highest degree of spatial and temporal symmetry while still manifesting a two-way eddy–mean flow interaction (i.e. with partially free evolution of the mean shear flow and stratification). This 'large-scale' flow has linear baroclinic instability modes, both force-balanced (Eady 1949) and anticyclonic–ageostrophic (Stone 1966; Molemaker, McWilliams & Yavneh 2005). The boundary conditions are horizontal periodicity and solid vertical boundaries with no stress or buoyancy flux (i.e. with no representation of turbulent boundary layers). Fluctuations amplify through these instabilities and equilibrate only by either viscous dissipation or an artificial fluctuation damping at the domain scale. The fluid dynamical model is the incompressible Boussinesq equations (BOUS).

This posing is designed to provoke a crisis in the sense that the fluctuation energy will continue to grow as the Reynolds number Re and domain size increase unless a forward energy cascade arises to provide an efficient 'interior' route to dissipation. The problem is solved in a parameter space with both Re and the Rossby number Ro as control parameters. To provide a comparison of dynamical standard, we also solve the equivalent problem with the force-balanced quasigeostrophic equations (QG), which is the asymptotic model as $Ro \to 0$ (Pedlosky 1987) where no forward cascade is expected as $Re \to \infty$.

This problem has a different focus compared with recent studies of randomly forced, strongly stratified turbulence by, among others, Lindborg (2005) and Waite & Bartello (2006). In those problems, with weak rotation (large Ro), there is a vigorous forward energy cascade. When Ro is decreased from large values, a certain degree of inverse energy cascade begins at an $O(1)$ threshold value. Our approach is very different and focuses on the strength of the forward cascade for small Ro. In other words, instead of focusing on the emergence of an inverse energy cascade as Ro is reduced, we study the emergence of a forward energy cascade when the Ro value characterizing the mean flow and its primary geostrophic instability has a small, finite value. The latter is the more geophysically relevant problem for the general circulation.

Section 2 explains the model formulation and solution methods. Section 3 presents solutions for the unforced spin-down of an Eady flow, and § 4 presents equilibrium solutions. Section 5 analyses departures from diagnostic force balances and their relation to forward energy cascade and fine-scale instability of density fronts. Conclusions are in § 6.

2. Formulation and methods

We pose the problem as the nonlinear evolution of fluctuations around a mean horizontal current $V(z)\hat{\mathbf{y}}$ in geostrophic, hydrostatic balance for a rotating, stably stratified fluid with Coriolis frequency $f(y) > 0$ and Brunt–Vaisalla or buoyancy frequency $N(z) > 0$. To focus on the primary issue, we assume here that f, N and $d_z V$ are spatially uniform, even though their variations are important for realistic, large-scale currents. Similarly, we ignore horizontal variations in V, which implies a linear horizontal variation of the hydrostatic, geostrophic buoyancy field $B(x)$. Boundary layers are avoided by assuming horizontal periodicity with zero horizontal average for the fluctuation fields and solid vertical boundaries without any momentum or heat flux. The configuration of horizontal fluctuation periodicity in the presence of a linear mean $B(x)$ requires a closure principle, which we choose as locally conservative

eddy–mean energy exchange. (This configuration is an ansatz for the central region of a broad baroclinic jet whose horizontal scale is much wider than the dominant fluctuation scale, e.g. the baroclinic deformation radius, L_r.) A price we pay for the simplicity of this degree of spatial homogeneity is that the mean flow and stratification must be artificially maintained in the face of their modification by eddy fluxes.

Since our focus is on possible departures from balanced flows, we will use BOUS for the fundamental fluid dynamics of an incompressible fluid. The problem considered is therefore a non-geostrophic, non-hydrostatic, non-conservative generalization of the linear-stability analysis in Eady (1949). Since an important goal is to assess the degree and importance of the loss of diagnostic force balance with respect to both the geostrophic and hydrostatic approximations, this investigation continues the instability analysis by Stone (1966, 1970) and Molemaker *et al.* (2005) into the turbulent equilibrium regime.

We derive non-dimensional equations using the following scales for the mean state and fluctuation quantities: horizontal domain width L, vertical domain height H, horizontal velocity V_0, time L/V_0, Coriolis frequency f, dynamic pressure and buoyancy $\rho_o f V_0 L$ and $f V_0 L/H$, hydrostatic pressure and buoyancy of the mean vertical stratification N^2H^2 and N^2H, vertical velocity fV_0^2/N^2H and energy density V_0^2. As a result several non-dimensional parameters appear: Rossby number $Ro = V_0/fL$; Froude number $Fr = V_0/NH$; aspect ratio $\lambda = H/L$; and $\epsilon = fLV_0/N^2H^2 = Fr^2/Ro$. This non-dimensionalization follows McWilliams (1985), and it is designed to expose the generally weak deviations of the flow from balance when these four parameters are not large.

The non-dimensional profiles for the mean meridional velocity and buoyancy field are

$$\left.\begin{aligned} V(z) &= S(t)\left(z-\frac{1}{2}\right), \\ B(x,z) &= \epsilon^{-1}\mathscr{B}(z,t) + S(t)\left(x-\frac{1}{2}\right). \end{aligned}\right\} \tag{2.1}$$

The domain is $[0, 1]$ in each coordinate. Note that S is the mean vertical shear, and $\mathscr{B} = \epsilon\overline{B}$ is the mean stratification, where the overbar denotes a horizontal average. The associated mean zonal and vertical velocities are zero. This mean flow satisfies hydrostatic, geostrophic balance, $\partial_z V = \partial_x B$, with as yet undetermined shear amplitude $S(t)$ and mean stratification profile $\mathscr{B}(z, t)$. The associated mean zonal and vertical velocities are zero. The values $S = \partial_z\mathscr{B} = 1$ are Eady's flow. In conservative dynamics, the potential vorticity is a Lagrangian invariant. Its spatial structure is relevant to possible flow instabilities. For BOUS (§ 2.1), the Ertel potential vorticity (non-dimensionalized by fN^2) for the mean state is

$$Q_m = \partial_z\mathscr{B} - Ro\,\epsilon\,S^2 \leqslant \partial_z\mathscr{B}. \tag{2.2}$$

The inequality indicates that Q_m has an anticyclonic constant value for Eady's flow.

2.1. *Boussinesq model*

The governing non-dimensional equations in BOUS apply to the horizontally averaged stratification and fluctuations about the geostrophic, hydrostatic shear flow $\propto S$ in

(2.1):

$$\left.\begin{aligned}
Ro\left(\partial_t u + [\boldsymbol{u}\cdot\nabla u]^\diamond + V\partial_y u\right) - v + \partial_x p &= \frac{Ro}{Re}\nabla^2 u - Ro\,\mathscr{R}_u,\\
Ro\left(\partial_t v + [\boldsymbol{u}\cdot\nabla v]^\diamond + V\partial_y v + \epsilon\, w\partial_z V\right) + u + \partial_y p &= \frac{Ro}{Re}\nabla^2 v - Ro\,\mathscr{R}_v,\\
Fr^2\lambda^2\left(\partial_t w + [\boldsymbol{u}\cdot\nabla w]^\diamond + V\partial_y w\right) + \partial_z p &= b + \frac{\epsilon Ro\lambda^2}{Re}\nabla^2 w - Fr^2\lambda^2\mathscr{R}_w,\\
\partial_x u + \partial_y v + \epsilon\partial_z w &= 0,\\
\partial_t b + \boldsymbol{u}\cdot\nabla b + V\partial_y b + uS + \alpha\left[b - \frac{(z-0.5)}{\epsilon}\right] &= \frac{Pr}{Re}\nabla^2 b - \mathscr{R}_b,
\end{aligned}\right\} \tag{2.3}$$

together with the boundary conditions of $w=0$ at $z=0, 1$ and horizontal periodicity for all fields. Note that u, v and w are cross-stream, downstream and vertical fluctuation velocity components with zero horizontal average, and $\boldsymbol{u}=(u, v, \epsilon w)$. p is pressure.

Note that $b = \mathscr{B}/\epsilon + b'$

is the periodic part of the buoyancy field with b' as the fluctuation field with zero horizontal average. Thus, b includes the periodic mean stratification but not the non-periodic mean horizontal trend, $S(x-0.5)$, in (2.1); the latter is determined separately from (2.13) below. The symbol $[\cdot]^\diamond$ denotes removal of the horizontal average momentum advection, which here is the divergence of the vertical Reynolds stress, $\epsilon\partial_z\overline{\boldsymbol{u}w}$. The definitions of Reynolds and Prandtl numbers are

$$Re = \frac{\nu}{V_0 L} \quad \text{and} \quad Pr = \frac{\nu}{\kappa},$$

and we choose $Pr=1$ for all cases. Explicit diffusion (hence dissipation) is incorporated into the model by means of the Laplacian operator ∇^2. In addition to this, the upwind-weighted discretization of the advection operator provides additional numerical dissipation (§2.3). The stratification is restored towards the uniform stratification in Eady's flow with a non-dimensional rate α. There are additional large-scale fluctuation damping terms $\mathscr{R}$ described in §4. The mean stratification balance can be extracted from (2.3) by horizontally averaging:

$$\partial_t\mathscr{B} = -\epsilon^2\partial_z\overline{wb'} + \frac{Pr}{Re}\partial_{zz}\mathscr{B} - \alpha(\mathscr{B} - z + 0.5), \tag{2.4}$$

with b' determined by the residual balance after subtracting (2.4) from (2.3). In a baroclinically unstable Eady flow with $\overline{wb'}>0$, the mean stratification will tend to increase (a.k.a. eddy restratification). The role of $\alpha>0$ is to balance this tendency and achieve an equilibrium stratification close to the Eady one even when Re is very large.

To accompany the fluctuation evolution (2.3), we require an equation for the mean shear $S(t)$. Since (2.1) is not strictly consistent with either horizontal periodicity nor an infinite horizontal extent, a closure hypothesis is needed, and we choose one comprised of a domain-averaged energy balance in the fluctuation–mean interactions and forcing terms that act to restore the evolving flow towards Eady's flow.

The kinetic energy density for the mean flow is $E_{km}=(1/2)V^2$, and its volume integral for $V(z)$ in (2.1) is

$$\mathscr{E}_{km} \equiv \overline{\langle E_{km}\rangle} = \frac{S^2}{24}, \tag{2.5}$$

where the angle brackets denote a vertical integral (also equal to a vertical average in a domain of unit height). The fluctuation equations (2.3) have an integral kinetic energy conservation law for

$$E_{kf} = \frac{1}{2}\left(u^2 + v^2 + \epsilon^2\lambda^2 w^2\right), \tag{2.6}$$

for example

$$\frac{\mathrm{d}\mathscr{E}_{kf}}{\mathrm{d}t} = \frac{\epsilon}{Ro}\overline{\langle wb'\rangle} - \epsilon\,\overline{\langle vw\rangle}\,S - D_{kf}, \tag{2.7}$$

with $\mathscr{E}_{kf} = \overline{\langle E_{kf}\rangle}$ and a dissipation rate D_{kf} that is the sum of numerical dissipation (§ 2.3) and explicit dissipation from the diffusion and damping forces.

Lorenz (1955) demonstrated that the energy exchange between a zonal mean flow S and its fluctuations is most cogently described in terms of conservation of kinetic $\mathscr{E}_k$ plus available potential $\mathscr{E}_a$ energies (rather than total potential energy, which in our problem is a function only of $\mathscr{B}$, not the mean flow S). Accordingly, we adopt an energy closure principle to determine the evolution of $S(t)$; i.e.

$$\frac{\mathrm{d}(\mathscr{E}_{km} + \mathscr{E}_{kf} + \mathscr{E}_a)}{\mathrm{d}t} = NCT, \tag{2.8}$$

where NCT generically denotes the non-conservative diffusive, damping and restoring-forcing terms. The term $\mathscr{E}_a$ is formally defined as the difference in the potential energy $\mathscr{E}_p$ of a given three-dimensional buoyancy field and the reference (lowest) potential energy $\mathscr{E}_{p_{ref}}$ that could be reached by an adiabatic rearrangement of parcels into a horizontally uniform field with non-negative vertical buoyancy gradient:

$$\mathscr{E}_a = \mathscr{E}_p - \mathscr{E}_{p_{ref}}. \tag{2.9}$$

In BOUS, no explicit expression for $\mathscr{E}_a$ is known because the rearranged reference profile cannot be specified *a priori*; nevertheless, following Winters *et al.* (1995), we introduce an operational procedure for determining $\mathscr{E}_a$ and its derivatives from the buoyancy field (Molemaker & McWilliams 2010). Furthermore, we can decompose $\mathscr{E}_a$ into mean and fluctuation contributions by

$$\mathscr{E}_a = \mathscr{E}_{am} + \mathscr{E}_{af}, \tag{2.10}$$

where $\mathscr{E}_{am}$ is evaluated using only the mean buoyancy field ($\mathscr{B}$, S) and $\mathscr{E}_{af}$ is evaluated by residual. Since $\mathscr{E}_a$ is a functional of S and b, we evaluate its time derivative by

$$\frac{\mathrm{d}\mathscr{E}_a}{\mathrm{d}t} = \frac{\delta\mathscr{E}_a}{\delta S}\cdot\frac{\mathrm{d}S}{\mathrm{d}t} + \frac{\delta\mathscr{E}_a}{\delta b}\cdot\frac{\partial b}{\partial t}. \tag{2.11}$$

The δ symbol denotes a functional derivative. The dots are vector products with the functional argument (note that S is zero dimensional and $b(x, y, z)$ is three-dimensional). Thus, the vector products in (2.11) are equivalent to volume integrals in the unit cube. In practice the functional derivatives are calculated by finite differences (as in the rest of the numerical model; § 2.3); e.g.

$$\frac{\delta\mathscr{E}_a}{\delta S} = \frac{\mathscr{E}_a[S + 0.5\mu,\, b] - \mathscr{E}_a[S - 0.5\mu,\, b]}{\mu}, \tag{2.12}$$

with μ a small number but large enough to avoid floating-point precision errors.

We now apply the energy closure principle (2.8) with an additional assumption about the role of the NCT, viz. its effects are partitioned into a restoring forcing of the mean shear flow (with the same rate α as in (2.4)) and its effects that follow from

the derivation of an energy balance relation for the periodic-component equations (2.3), which are thus assigned to the energy balance of this component. Thus, the principle yields an energy balance equation for $S(t)$ that is forced by the restoring term and by the conservative–dynamical exchanges with the periodic flow components so that the mean–eddy conversion terms that appear in the periodic-component energy-balance equations are subtracted from the S energy balance equation; i.e.

$$\frac{\mathrm{d}(\mathscr{E}_{km}+\mathscr{E}_{am})}{\mathrm{d}t} = -\frac{\mathrm{d}(\mathscr{E}_{kf}+\mathscr{E}_{af})}{\mathrm{d}t}$$

with respect to these conversion terms. In equilibrium (§4), the conversion terms act as sinks of mean-flow energy. By combining (2.3), (2.5), (2.7), (2.8) and (2.11), we obtain

$$\left(\frac{S}{12}+\frac{\delta\mathscr{E}_a}{\delta S}\right)\left(\frac{\mathrm{d}S}{\mathrm{d}t}-\alpha(1-S)\right) = \frac{\epsilon}{Ro}\overline{\langle wb'\rangle}-\epsilon\overline{\langle vw\rangle}S-\frac{\delta\mathscr{E}_a}{\delta b}\cdot(\boldsymbol{u}\cdot\nabla b+V\partial_y b+Su). \tag{2.13}$$

The set (2.3) and (2.13) provides a well-posed system for the evolution of the mean state and fluctuations. In §2.2, we show that this system is asymptotically consistent with the more familiar QG model where $\mathscr{E}_a$ and its derivatives are analytically specifiable (Molemaker & McWilliams 2010). In (2.13), the conversion of energy from mean to fluctuations is balanced by a reduction of S. Because of the dissipative terms in the fluctuation equations, this system will eventually spin down to rest in the absence of restoring forcing (§3), and it will achieve equilibrium with a finite S value when α is non-zero.

The fluctuation Ertel potential vorticity is $Q_f = Q - \overline{Q}$. In the absence of forcing and dissipative effects, Q is conserved following the flow. Since the initial and mean states have no interior horizontal Q gradients, the fluctuations do not inherit any Q variations through the instability generation process. However, the model equations do not exactly conserve Q in their discrete form, and viscous and diffusive effects can generate Q fluctuations in the flow, mainly on small scales. (Indeed, it is hard to imagine any turbulent flow with Boussinesq dynamics that would retain an exactly uniform Q field.) Because of the tendency of Q to homogenize on horizontal or isopycnal surfaces by eddy mixing (Rhines & Young 1982), we expect its interior horizontal gradients to remain small and find that this is generally so. In particular, we do not see any correspondence in our solutions between the structure of Q on large and intermediate scales and the outbreak of instabilities on finer scales; in this sense, we believe that our problem posing provides a valid representation of Boussinesq turbulence in an Eady-like flow. Because we do allow an evolution of the mean stratification profile $\mathscr{B}(z)$ through eddy restratification flux in (2.4), there is similarly an evolution in $\overline{Q}(z)$; however, we do not believe that this feature makes a fundamental difference in the BOUS turbulent equilibrium dynamics.

2.2. *Quasigeostrophic model*

Starting with (2.3), take the curl of the horizontal momentum equations, use the hydrostatic approximation, add the vertical derivative of the buoyancy equation, discard all terms that are asymptotically small in Ro, Fr and ϵ, and neglect vertical diffusion. The result is the non-dimensional, QG potential vorticity equation for the fluctuations, including horizontal diffusion:

$$[\partial_t + V\partial_y]q + J_h(\Psi, q) = \frac{1}{Re}\nabla_h^2 q - \mathscr{R}_q, \quad q = \nabla_h^2\Psi + \frac{\epsilon}{Ro}\,\partial_{zz}\Psi. \tag{2.14}$$

Here, q is the QG potential vorticity, and Ψ is the geostrophic streamfunction with $u=-\partial_y\Psi$, $v=\partial_x\Psi$. (With this QG definition of potential vorticity, the mean Eady flow (2.1) has zero q; cf. Q_m in (2.2).) The subscript h denotes a horizontal Laplacian operator. The vertical velocity is $w=-[\partial_t+V\partial_y]\partial_z\Psi+J_h(\Psi,\partial_z\Psi)$, and the buoyancy is $b=\partial_z\Psi$. Boundary conditions at $z=0$, 1 are

$$[\partial_{tz}+V\partial_{zy}]\Psi+J_h(\Psi,\partial_z\Psi)-S\partial_y\Psi=\frac{1}{Re}\nabla_h^2\partial_z\Psi-\mathscr{R}_b. \tag{2.15}$$

Because of the linear homogeneous operator form of the potential vorticity equation in (2.14) (with $\mathscr{R}_q\propto q$), q will remain zero at all times if it is initially zero. This is the class of solutions we focus on. For QG solutions with $q=0$ in the interior, the dynamics is that of two coupled surface quasigeostrophic models (SQG), each one representing the buoyancy advection–diffusion dynamics at one of the vertical boundaries (Held *et al.* 1995). Baroclinic instability is permitted through the coupling of vertical edge waves (Eady 1949). For horizontal scales small compared to L_r (the first-baroclinic deformation radius), the coupling is weak, and the dynamics reduce to uncoupled SQG models associated with each of the boundaries. Thus, the structure of the turbulent flow at submesoscales is consistent with that of Held *et al.* (1995).

In QG, the stratification remains fixed at its Eady value of $\mathscr{B}=1$, and its eddy-induced evolution rate is $\mathcal{O}(\epsilon^2)$. An energy equation for the fluctuations is obtained by multiplying (2.14) by $-\Psi$ and integrating over the domain. After using the boundary conditions and making several integrations by parts, we obtain the following:

$$\left.\begin{aligned}\frac{\mathrm{d}\mathscr{E}_{qf}}{\mathrm{d}t}&=-\frac{\epsilon}{Ro}S\,\overline{\langle\partial_y\Psi\,\partial_z\Psi\rangle}-\frac{1}{Re}\left[\overline{(\nabla_h^2\Psi)^2}+\frac{\epsilon}{Ro}\overline{(\partial_z\nabla_h\Psi)^2}\right],\\ \mathscr{E}_{qf}&=\frac{1}{2}\overline{\langle(\partial_x\Psi)^2\rangle}+\overline{(\partial_y\Psi)^2}+\frac{\epsilon}{Ro}\overline{(\partial_z\Psi)^2}.\end{aligned}\right\} \tag{2.16}$$

The first term in $\mathscr{E}_{qf}$ is the QG approximation to $\mathscr{E}_{kf}$, and the second term is the contribution of the buoyancy fluctuations to $\mathscr{E}_a$. The corresponding expression for the mean QG energy is

$$\mathscr{E}_{qm}=\frac{S^2}{24}\left(1+\frac{\epsilon}{Ro}\right), \tag{2.17}$$

again a sum of $\mathscr{E}_{km}$ and the mean-flow contribution to $\mathscr{E}_{am}$. (This expression is consistent with (2.16) for a mean streamfunction $\Psi_m=S(z-(1/2))\,(x-(1/2))$.) With a closure principle of conservation of $\mathscr{E}_{qf}+\mathscr{E}_{qm}$ with respect to fluctuation–mean conversion terms, and a restoring force towards Eady's flow, the QG equation for $S(t)$ is

$$\frac{S}{12}\left(1+\frac{\epsilon}{Ro}\right)\left(\frac{\mathrm{d}S}{\mathrm{d}t}-\alpha(1-S)\right)=\frac{\epsilon}{Ro}S\,\overline{\langle\partial_y\Psi\,\partial_z\Psi\rangle}. \tag{2.18}$$

The use of available potential energy in the closure equation for S assures that QG formulation (2.18) is the limiting form of BOUS (2.13) as $Ro\to 0$ (and ϵ/Ro remains $O(1)$). (This follows from $\delta\mathscr{E}_a/\delta S=(\epsilon/Ro)(S/12)$ and $\delta\mathscr{E}_a/\delta b=\epsilon b/Ro$ by (2.16) and (2.17). The second right-hand-side term in (2.13), work by vertical Reynolds stress, is $O(\epsilon)$ and disappears. The third right-hand-side term becomes in this limit $-(\epsilon/Ro)\int\int\int b(\boldsymbol{u}\cdot\nabla b)=-(\epsilon/Ro)\overline{\langle wb'\rangle}$, the conversion of potential into kinetic energy, which cancels the first right-hand-side term. The fourth right-hand-side term $(\epsilon/Ro)\int\int\int Vb\partial_y b$ has zero integral due to the horizontally periodic boundary conditions. The final term of (2.13) becomes $-(\epsilon/Ro)S\int\int\int b'u$, which is the same as the lone conversion term in (2.18).)

Apart from its asymptotic dynamical approximations, this posing for the QG model has two structural differences compared to BOUS. One is that the mean stratification does not evolve away from the Eady state, $\mathscr{B} = 1$, although the mean shear amplitude $S(t)$ does change. The other is that the interior q remains exactly zero, corresponding to a spatially uniform Q equal to $1 - Ro^2 S(t)$ in (2.2) (rather than the limited Q variations that do arise in BOUS; end of § 2.1). While one could reduce at least the first difference by adopting the time-averaged $\mathscr{B}(z)$ from BOUS in the QG model, it would make less simply formulated QG comparison standard, and, more importantly, we do not believe this change would materially affect the character of the BOUS-QG comparisons in § 3–4.

2.3. *Computational methods*

The code for BOUS uses finite-difference discretization. It has previously been used to compute laboratory scale flows (Molemaker, McWilliams & Yavneh 2000) and atmospheric and ocean flows at scales of tens of kilometres (Molemaker & Vilá-Guerau de Arellano 1998; Molemaker & Dijkstra 2000). Most of the spatial operators are centred schemes with second-order accuracy. It uses a QUIICK algorithm for advection of velocities and scalars (Leonard 1979). The QUICK scheme approximates fluxes across cell boundaries with third-order accuracy and introduces a small amount of numerical dissipation that has a truncation error functionally equivalent to a biharmonic operator; hence it is more scale selective than the Laplacian diffusion (Shchepetkin & McWilliams 1998). A three-dimensional multigrid Poisson solver allows it to run efficiently on large grids. A third-order Adams–Bashforth scheme is used to advance the variables in time. The model has no normal flow at $z = 0$ and 1 and periodic boundary conditions in the horizontal directions. In (2.9), the evaluation of the reference potential energy $\mathscr{E}_{p_{ref}}$, the lowest potential energy that can be reached through adiabatic rearrangement, is done with an efficient heap sort (Press *et al.* 1986) of the discretized buoyancy field following the procedure of Winters *et al.* (1995) (also see Molemaker & McWilliams 2010).

The QG code is designed as a companion to the BOUS code. It advances (2.14) in the interior and (2.15) for $\partial\Psi/\partial z$ at the top and bottom boundaries. Like its BOUS, it employs central differences for the Laplacian operator and a multigrid Poisson solver for Ψ on the three-dimensional grid, a QUICK algorithm for the advective terms and an Adams–Bashforth scheme for time stepping.

In both codes the total diffusive effects are a combination of the explicit diffusion operators in (2.3) and (2.14) and the implicit non-conservative effect of the QUICK algorithm that leads to a dissipation that is somewhat more scale selective than the Laplacian diffusion operator. To diagnose the contribution from the latter, we can compare the QUICK advection term with a centred, second-order scheme that is non-dissipative. Spectral energy balances (§ 4.3) are used to verify the correctness of these estimates. The total discrete dissipation (numerical plus explicit) D_{kf} is diagnosed using a discrete equation for kinetic energy, analogous to (2.7). For instance, the domain-integrated dissipative effect of advection can be computed by

$$D_{adv} = \int\int\int \boldsymbol{u}\cdot(\boldsymbol{u}\cdot\nabla\boldsymbol{u})\,\mathrm{d}x\,\mathrm{d}y\,\mathrm{d}z. \tag{2.19}$$

For a non-dissipative advection scheme, D_{adv} will be identically zero. Using an upwind-weighted advection scheme, $D_{adv} > 0$. By comparing D_{adv} with $D_{visc} = Re^{-1}\,\boldsymbol{u}\cdot\nabla^2\boldsymbol{u}$, we can assess the relative importance of each for the total dissipation. For all results, the explicit viscosity is chosen such that numerical and explicit dissipation are roughly

comparable. This estimation is used to compute an approximate effective Reynolds number for the flows computed. The viscosity ν_{eff} used to compute the approximate $Re_{eff} = V_0 L/\nu_{eff}$ is determined diagnostically as the ratio of the total dissipation and the horizontal shear variance (also see § 4.3). The total amount of dissipation is kept to a minimum since we want to study the capacity of the solutions to reach the smallest dissipative scales. The explicit diffusion coefficient is reduced with increasing resolution to allow increasing Re values while still maintaining smoothness on the grid scale, and this reduction occurs automatically with QUICK. The highest three-dimensional resolution used is a $512 \times 512 \times 128$ grid, corresponding to an estimated Reynolds number of $Re_{eff} = 6600$.

2.4. *Parameter regime*

On the basis of the Eady mean state and the domain dimensions, we choose the parameter values for a standard case as $Ro = 0.05$, $Fr = 0.5$ and $\lambda = 0.1$. The associated non-dimensional, first-baroclinic deformation radius is $L_r = 0.1$. Since baroclinic instability has a horizontal length scale close to L_r, it is perhaps more meaningful to interpret this choice in terms of an instability-scale Rossby number, $Ro_r = V_0/f L_r = Ro(L/L_r) = 0.5$. We might further rescale Ro and Fr by a factor of $S(t) < 1$ to reflect the actual mean flow strength that emerges in our solutions, although this would make only a modest fractional reduction. Thus, $Ro_r = Fr$, which is consistent with the conventional quasigeostrophic regime (often expressed as unit Burger number); however, the value of 0.5 is not asymptotically small, so we can expect important differences between the BOUS and QG solutions, which is a primary goal of the paper. Non-asymptotic values are typical of the core of the Gulf Stream and Jet Stream, although their shear and stratification profiles are not the same as in the Eady state. The value of λ is small but not as small as typical of the general circulations. In § 4, we investigate the effect of varying Ro and Fr, holding their ratio fixed. In QG, the solution does not depend explicitly on the Ro and Fr values but only on their squared ratio ϵ/Ro, and the QG solution is independent of the value of λ. Since our scientific focus is on the connection between the larger mesoscales where the primary Eady-flow instability occurs and the smaller submesoscales in equilibrium, the computational requirements are substantial, and we are practically constrained in our parameter choices away from asymptotically small values of Ro, Fr and λ. Relevant values of Rossby and Froude numbers for the fluctuations are discussed in § 4.2. Finally, because of the isotropic non-dimensional Laplacian diffusion operator in (2.3), the ratio of dimensional vertical and vertical diffusvities is equal to λ^2. The numerical values are expressed in terms of the effective Reynolds number Re_{eff} (§ 2.3) and are reported in § 3–4 in conjunction with specific grid configurations.

3. Spin-down

To illustrate the behaviour of our formulation for the mean-state evolution, we examine a set of spin-down experiments with no restoring forcing and initially small fluctuations. Companion solutions are computed using BOUS and QG.

During the initial phase of the evolution, the mean state is baroclinically unstable and loses energy to the fluctuations primarily at horizontal wavenumber $k = 2$ (i.e. a radian length scale of $L = 1/4\pi = 0.08$). Because of the small wavenumber of the unstable perturbation, the solution is initially only weakly dissipative, and the sum of mean and fluctuation energy is conserved through (2.8) with (2.13) and (2.18) (figure 1). After a period of transition during which dissipative terms attain significant

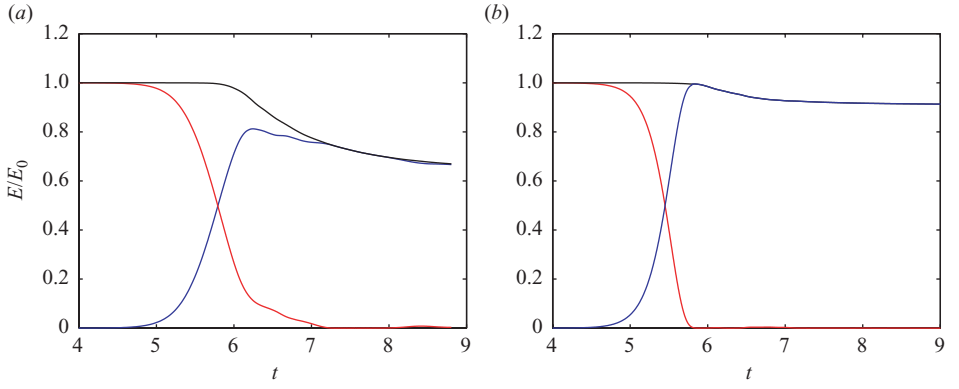

FIGURE 1. Evolution of total energy (kinetic plus available potential) in spin-down ($Re_{eff} = 2200$): (*a*) BOUS ($Ro_r = Fr = 0.5$); (*b*) QG. Blue is the fluctuation energy, red is the basic-state energy, and black is the total energy. Towards the end of the simulation, all the kinetic and available potential energy from the basic state is depleted, and the fluctuations have evolved towards a flow structure that fills the domain and is only weakly dissipative.

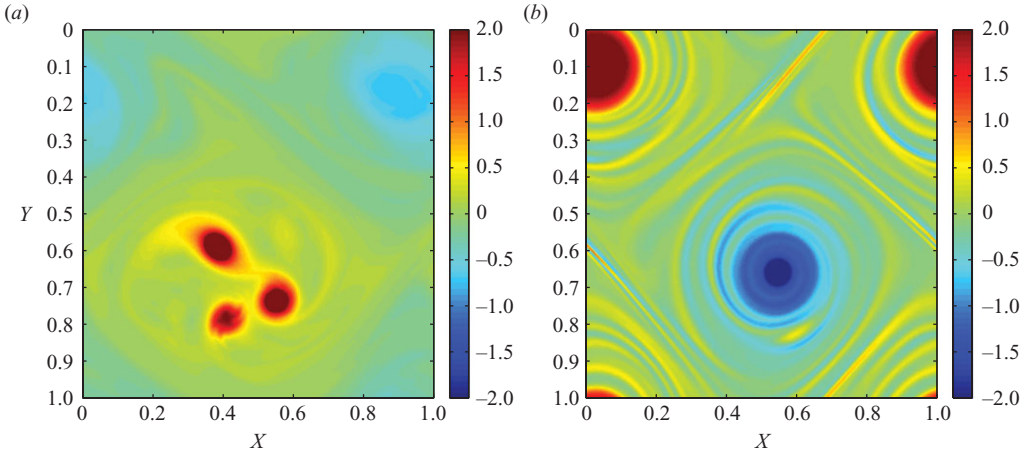

FIGURE 2. Vertical vorticity $\zeta^z(x, y)$ at $t = 9$ and $z = 0.5$ in spin-down ($Re_{eff} = 2200$): (*a*) BOUS ($Ro_r = 0.5$), where the fluctuations have evolved to a set of co-rotating cyclonic eddies; (*b*) QG, where the fluctuations have evolved to a dipole vortex structure.

amplitudes, the mean state is depleted ($S \to 0$), and the fluctuations continue to evolve without further energy input.

After the fluctuations reach large amplitude and self-advection matters, there is a period of intense frontogenesis in both BOUS and QG. Frontogenesis by a deformation field acting to sharpen the buoyancy gradients leads to a restratifying secondary circulation around the front that converts potential to kinetic energy (Hoskins & Bretherton 1972). This process is reflected in energization of small-scale flow components and increased dissipation rate. At the same time an inverse cascade of fluctuation energy occurs and leads to the formation of domain-filling vortices. A quasi-steady end state for the freely decaying fluctuations is dominated by the large-scale vortices that have little further energy cascade and weak dissipation. Snapshots of vorticity at $z = 0.5$ are in figure 2 for times corresponding to these end states.

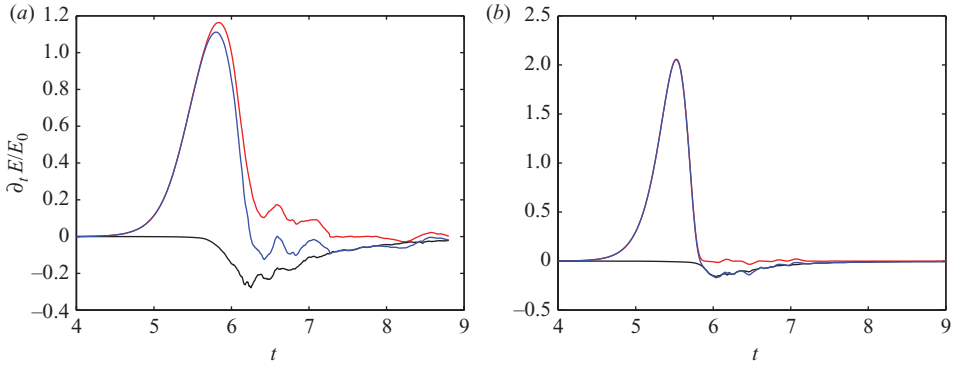

FIGURE 3. Energy balance for the fluctuations in spin-down ($Re_{eff} = 2200$): (a) BOUS ($Ro_r = 0.5$); (b) QG. Blue is the total rate of change of the fluctuations, red is the energy conversion from mean to fluctuations, and black is the dissipation of fluctuation energy.

The occurrence and disappearance of small scales, evidenced by a period of enhanced dissipation, is the result of a complicated process of frontogenesis, frontal instability, inverse and forward energy cascades, and selective dissipation of small scales (further discussed in §§ 4 and 5). The outcome of these processes is clearly seen in the difference in energy between the initial and end states (figure 1).

Figure 3 shows the energy transfer from the mean flow to fluctuations and dissipation during spin-down with an energy budget for the fluctuations. The rate of change of fluctuation energy indicates initial growth of the fluctuations when the mean state is unstable and baroclinic instability sets in. This is also evident from the energy transfer from mean to fluctuations that indicates a continuing energy source for the fluctuations up to the point where the mean state is almost fully depleted. Initially, the rate of change of fluctuation energy and energy transfer is nearly indistinguishable because of a very weak dissipation rate for total energy. The dissipation rate starts out very small when the fluctuation is dominated by the $k = 2$ baroclinic instability; it is large during the period of forward energy cascade through frontogenesis and small-scale instability, and it is weak again during the final stage where the flow is dominated by very large scales.

This paper focuses on the dynamical differences between QG (balanced) and BOUS solutions, and the implications for the efficiency of energy dissipation by fluctuation currents. The net energy loss in spin-down as a function of Re_{eff} is shown in figure 4. As discussed in § 2.1, the effective Re_{eff} for the solutions is a function of resolution; it is diagnosed *a posteriori* through an analysis of the combined dissipative effect of the numerical QUICK advection scheme and the explicit Laplacian diffusion. It is clear that for increasing Re, the energy dissipation for BOUS approaches a finite asymptotic value. The behaviour is markedly different in QG where the net energy loss becomes systematically smaller as Re_{eff} increases. This indicates that even though QG dynamics is capable of a certain amount of forward energy cascade for any finite Re_{eff} value, this route to dissipation has only a limited duration and efficiency when the dissipative scales are moved to higher wavenumbers with increasing Re_{eff}. This is very different for BOUS dynamics, where the forward energy cascade remains efficient enough to reach the dissipative scales even when diffusion moves to smaller scales. This result provides support for the idea that balanced dynamics is limited in its capacity to efficiently dissipate its energy and the idea that unbalanced dynamics is

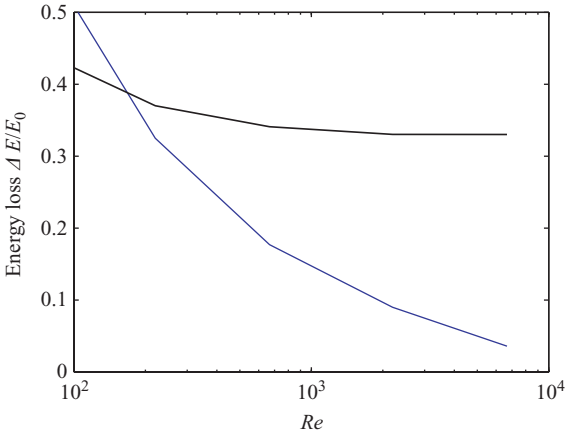

FIGURE 4. Total energy loss during spin-down for different values of Re_{eff}: BOUS ($Ro_r = 0.5$, black) and QG (blue).

essential for this route to dissipation to be viable at large Re_{eff}. The energy cascades for BOUS and QG are further studied in § 4.3.

4. Equilibrium

To go beyond the energy loss during a spin-down experiment, we now study equilibrated flows in which a sustained energy dissipation balances the energy input. For a given rate of restoring forcing, the solutions are allowed to evolve to a statistically stationary state with an energy input and dissipation balance on average. The mean state is being restored to the Eady flow with a non-zero value for α (§ 2). The value of α is chosen to approximately equal the growth rate of the most unstable baroclinic-instability mode for the initial mean state.

Furthermore, since the equilibration dynamics are characterized by a vigorous inverse cascade of fluctuation energy towards the largest scales, we are forced to include a damping term that removes energy at the smallest wavenumber at a rate of α_k. This is accomplished with the $\mathscr{R}$ operators in (2.3) and (2.15), where the horizontal Fourier transform of, for example $\mathscr{R}_u$ is equal to $-\alpha_k \hat{u}(k_x, k_y)$ when $k_h = \sqrt{(k_x^2 + k_y^2)} < 2$. Note that $\hat{u}$ is the complex Fourier amplitudes of u. This additional damping is introduced to avoid solutions that are dominated by the largest available scales (smallest wavenumbers) because of the ever-present inverse energy cascade in both BOUS and QG. However, the damping coefficient is chosen to be small enough to prevent this form of dissipation from being the primary one. With these considerations, the value is chosen to be $\alpha_k = 0.2$, leading to an almost equal partition between $\mathscr{E}_{kf}$ dissipation at high and low wavenumbers for the high-Re BOUS solutions. Because we find that QG has a more efficient inverse energy cascade than BOUS, we choose the larger $\alpha_k = 0.6$ to have the QG equilibrium fluctuation energy generation rate equal to BOUS for high-Re values (figure 6). However, independent of the choices for α_k, our primary result is robustly true: with high-Re values, the small-scale dissipation efficiency in QG is much less than that in BOUS (figure 11). Finally, because the fluctuation dynamics are characterized by restratification ($\overline{w'b'} > 0$ and increased $\partial_z \mathscr{B}$, especially near the boundaries), the $\mathscr{R}_b$ operator contains point-wise restoring to the Eady profile, $\alpha(b - z/\epsilon)$, that acts on both $\mathscr{B}$ in (2.4) and b', to prevent this term from

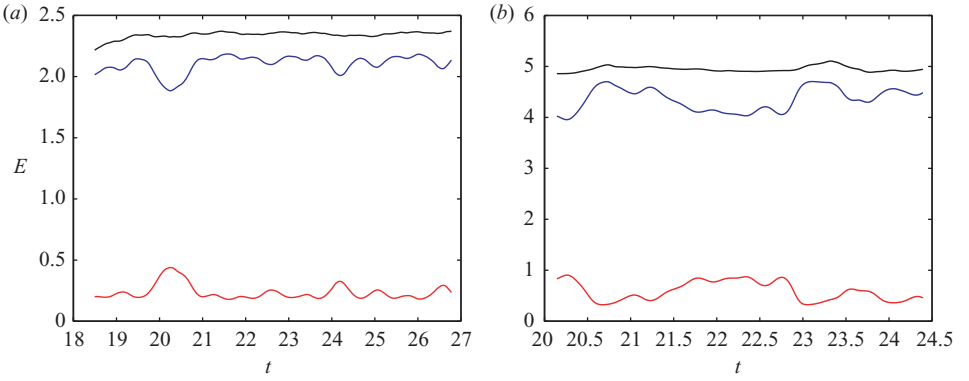

FIGURE 5. Time series of total kinetic plus available potential energy (black) and its mean (red) and fluctuation (blue) components for $Re_{eff} = 2200$ with restoring forcing during equilibrium: (*a*) BOUS ($Ro_r = 0.5$); (*b*) QG.

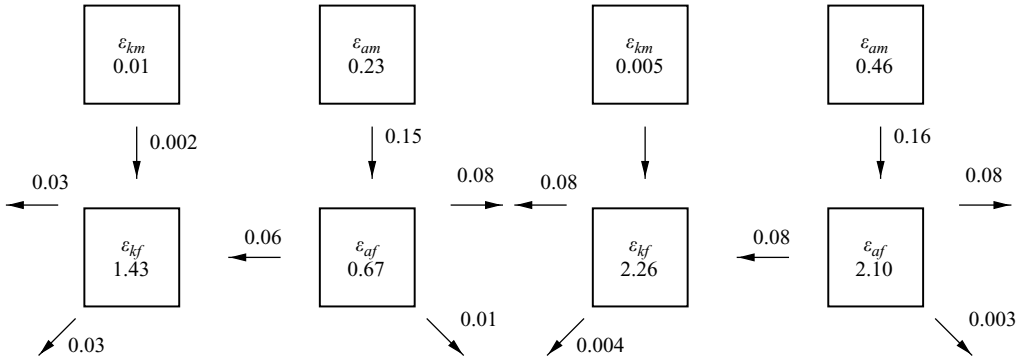

FIGURE 6. Averaged energy balance in equilibrium ($Re_{eff} = 6600$): (left four boxes) BOUS ($Ro_r = 0.5$); (right four boxes) QG. All values are scaled with the initial total energy of the basic state E_0. The boxes indicate the energy content (i.e. $\mathscr{E}_{km}$ in upper left, $\mathscr{E}_{am}$ in lower left, $\mathscr{E}_{kf}$ in upper right and $\mathscr{E}_{af}$ in lower right), and the arrows indicate the energy tendencies. Arrows between boxes are conversion terms. Lateral-outward arrows indicate dissipation by the low-wavenumber damping, and diagonal-outward arrows indicate small-scale dissipation. The mean-restoring work arrow is not drawn; its magnitude is equal to the sum of all the energy loss terms.

pushing local regions with weakly stable stratification towards unstable stratification (i.e. $\partial_z b < 0$).

The figure 5 time series for total energy are for BOUS (figure 5*a*) and QG (figure 5*b*) during a time period after statistical equilibrium has been established. There is noticeable variability in the mean and fluctuation energy levels, mainly at the time scale of the larger eddies in the solutions. Variations in the total (mean plus fluctuations) energy are much smaller.

Energy diagrams show the very different ways in which BOUS and QG manage to equilibrate (figure 6). In BOUS, the mean state provides a sustained source of energy for the fluctuations through a horizontal Reynolds stress (0.002) and a conversion from mean available potential to fluctuation available potential energy (0.15). This is consistent with the interpretation that the main source of energy of the fluctuations is the baroclinic instability of the mean state. About half of the energy that arrives

as fluctuation $\mathscr{E}_a$ is removed by restoring forcing of the buoyancy field and damping of the largest scales of the fluctuations. An additional amount (about 10 %) is dissipated as $\mathscr{E}_a$, and the remainder is forcing the fluctuation $\mathscr{E}_k$ through the release of potential energy by the buoyancy flux $\overline{wb'}$. From the perspective of $\mathscr{E}_{kf}$, the energy input by Reynolds stress and the release of potential energy is balanced by the damping of low wavenumbers (0.03) and dissipation of $\mathscr{E}_{kf}$ (0.03). For the experiments with high Re_{eff}, the dissipation occurs at increasingly high wavenumber, and non-zero dissipation implies a forward cascade of energy (§ 4.3). These results, therefore, indicate a sustained forward energy flux that is a significant fraction of the inverse energy cascade. In contrast, the QG solution is characterized by an equilibrium where all the energy put into the fluctuations through the mean state is removed at the smallest wavenumber through the low-wavenumber restoring term (α_k). No sustained forward energy cascade is established neither in the kinetic energy nor in the available potential energy. As a result, no internal dissipation is accomplished in QG, and, without the large-scale damping, the solution would not be able to equilibrate without having unrealistically large flows. The different types of energy balance and the corresponding exchanges of energy for BOUS and QG implied by figure 6 are central to this paper and are further discussed in §§ 4.2, 4.3 and 5.1.

4.1. *Flow structure: fronts and boundary effects*

Snapshots for ζ^z and b during statistical equilibrium near the upper boundary are shown in figure 7. For the vertical component of vorticity, both solutions show filamentation and the occurrence of sharp gradients (i.e. fronts). The difference between BOUS and QG is most evident in the appearance of small-scale fluctuations around frontal regions in BOUS that are absent in QG. The horizontal scale of these BOUS features is very small, about 10 % of L_r; in § 5.2 we show how they act to limit frontal sharpness.

The horizontally averaged buoyancy profile during statistical equilibrium for BOUS is plotted in figure 8. (The QG solution does not allow for the mean stratification to change from $N^2 = \partial_z \mathscr{B} = 1$.) Because of the continuing release of potential energy by the fluctuations, the averaged stratification is larger, by about a factor of 2, than the initial stratification of the basic state. Without a restoring term in the buoyancy equation (2.4), the average stratification would keep increasing, and this would result in an increasing L_r. For large enough L_r, the basic state would cease to be unstable to baroclinic instabilities. Evident in the $\mathscr{B}$ profile is the moderate increase in stratification near the top and bottom boundary, indicating a modest intensification near the surface. This stratification enhancement accompanies fluctuation intensification near the boundaries in the buoyancy b and vertical vorticity ζ^z (figure 9). On the other hand, even without the stratification enhancement, QG shows a much stronger degree of fluctuation intensification near top and bottom boundaries, especially in ζ^z. This behaviour is not uncommon in SQG models where all dynamics arise from the top and bottom surfaces. The profiles of w_{rms} differ even more; QG has a sharp increase of w_{rms} towards the surface, whereas the BOUS w_{rms} smoothly decreases towards zero. Both QG and BOUS show increased frontal activity near the boundary, as indicated by the amplitude for $|\nabla b|$, but for QG the contrast between boundary and interior is much more pronounced. Interior ∇b_{rms} is 50 % of its boundary value for BOUS, but it is only 5 % of its boundary value for QG. The probability density functions (PDFs) for the strength of buoyancy fronts, as indicated in $|\nabla b|$, are plotted in figure 10. The PDFs for BOUS and QG have longer tails near the boundary than in the interior, indicating stronger boundary fronts. For QG there is essentially no interior

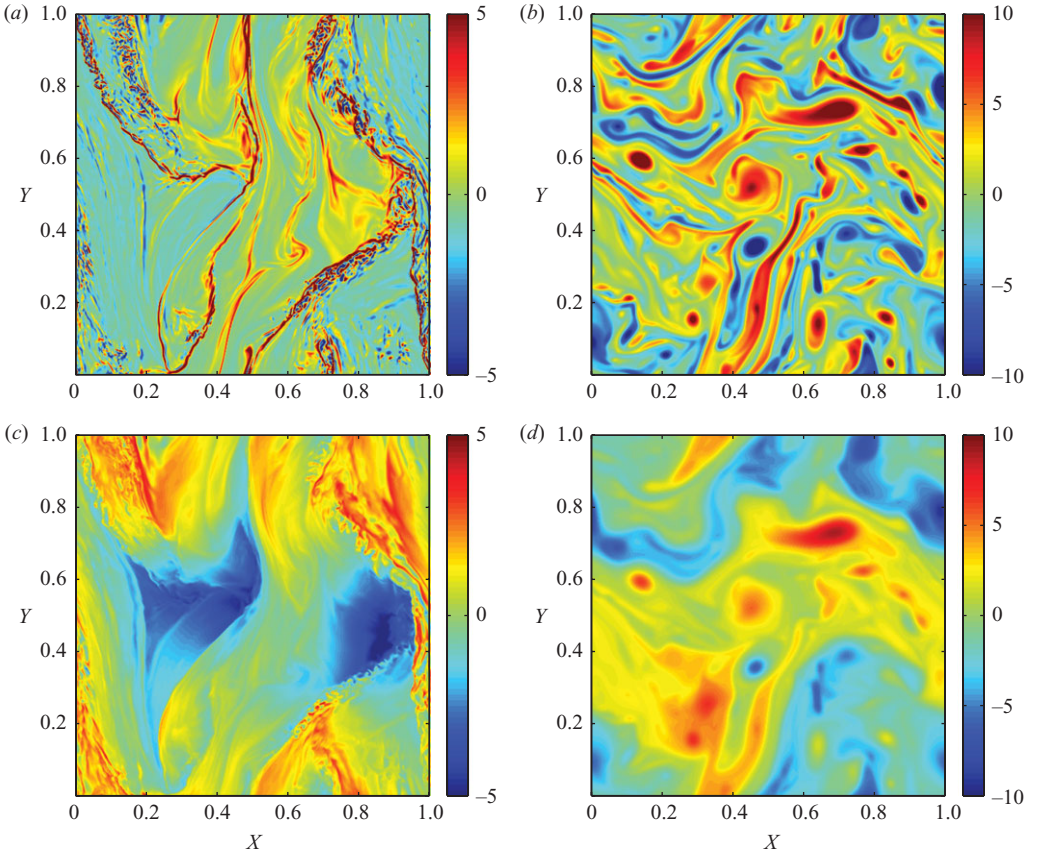

FIGURE 7. Snapshots in equilibrium ($t = 100$) at $z = 0.96$ for $Re_{eff} = 2200$: BOUS ($Ro_r = 0.5$) ζ^z (a) and b (c); the same for QG in (b,d). Note the fine-structure present in BOUS.

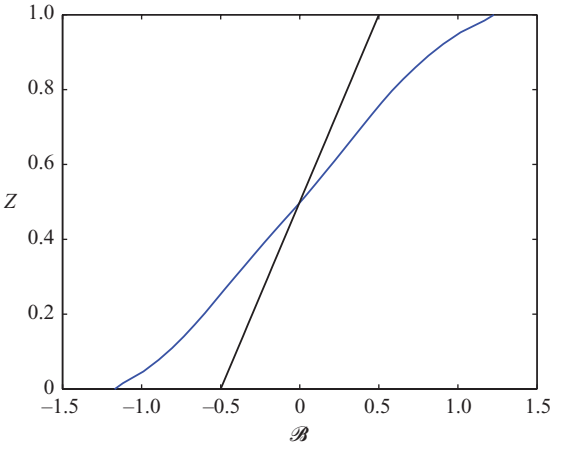

FIGURE 8. Mean buoyancy profile $\mathscr{B}$ in BOUS ($Ro_r = 0.5$, $Re_{eff} = 2200$): black is the basic-state stratification (equal to the permanent QG stratification), and blue is the averaged stratification after equilibration.

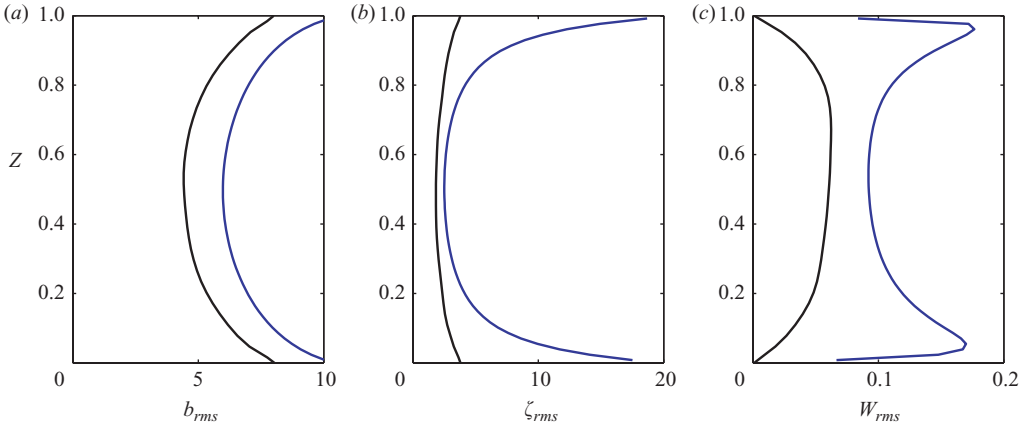

FIGURE 9. RMS profiles of b, ζ^z and w in equilibrium ($Re_{eff} = 2200$): BOUS ($Ro_r = 0.5$, black) and QG (blue).

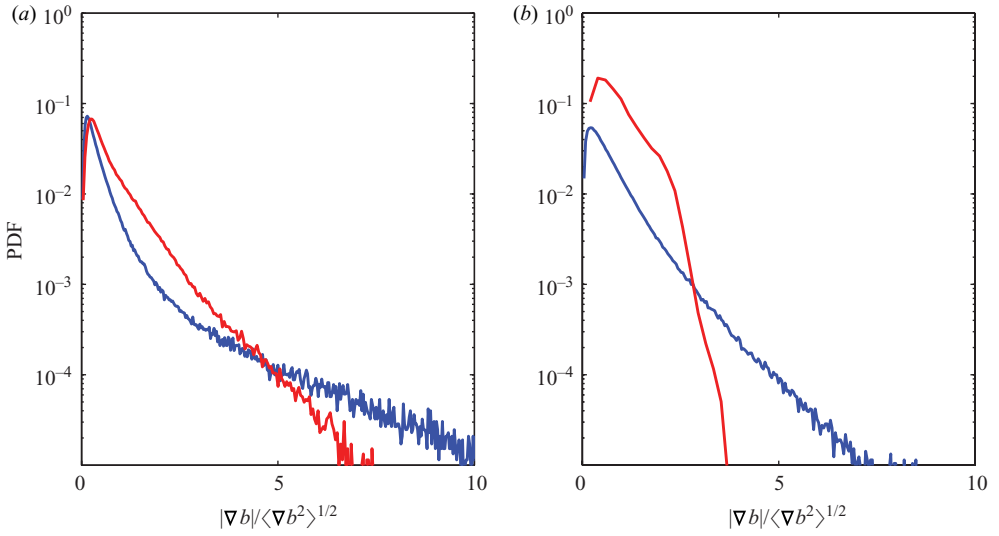

FIGURE 10. PDF of $|\nabla b|$ in the interior (red) and near the boundary (blue) ($Re_{eff} = 2200$): BOUS ($Ro_r = 0.5$, a) and QG (b). The PDF is normalized to have unit integral and unit variance. The interior is defined as $0.375 < z < 0.625$, and the near-boundary as $z < 0.125$ or $z > 0.875$. Average r.m.s. values are $\nabla b_{rms} = 0.51$ (BOUS interior), $\nabla b_{rms} = 1.11$ (BOUS near-boundary), $\nabla b_{rms} = 0.05$ (QG interior) and $\nabla b_{rms} = 1.07$ (QG near-boundary).

frontogenesis. Note that the boundary PDF for BOUS falls off somewhat faster than QG for intermediate frontal amplitudes but extends farther towards extreme amplitudes. This result is consistent with earlier work (Held *et al.* 1995), where SQG models do exhibit frontogenetic processes. However, our results demonstrate that the strength of frontogenesis is weaker in QG compared to BOUS.

4.2. *Dissipation efficiency and fluctuation Rossby number*

An equilibrated flow requires a balance between forcing and dissipation. If the dissipation is to occur at a very small scale, an efficient energy cascade has to be established so that the energy input at large scales can reach the small scales.

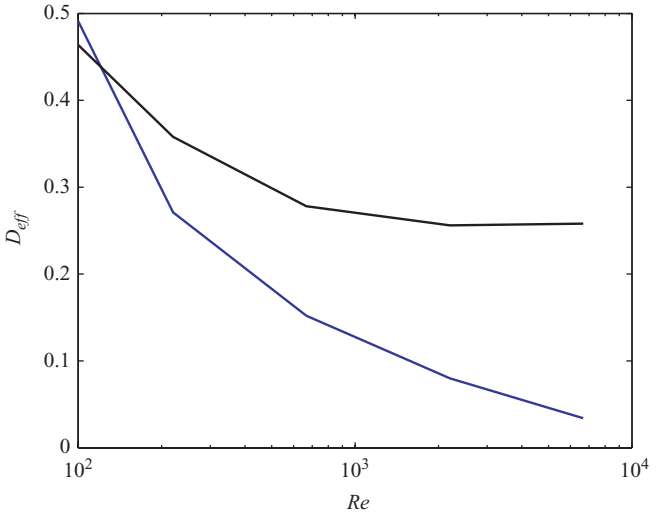

FIGURE 11. Dissipation efficiency as a function of Re_{eff}: BOUS ($Ro_r = 0.5$, black) and QG (blue).

We introduce the dissipation efficiency D_{eff} defined by

$$D_{eff} = \frac{\mathscr{D}_f}{\mathscr{E}_{kf}}. \tag{4.1}$$

Here, D_{eff} is the volume-integrated, small-scale, fluctuation dissipation rate $\mathscr{D}_{kf}$, due to both viscous and numerical diffusion, divided by the integrated fluctuation kinetic energy $\mathscr{E}_{kf}$. A small value of D_{eff} indicates a solution with a relatively inefficient forward energy cascade and, consequently, a poor dissipation efficiency.

Figure 11 plots D_{eff} as a function of Re_{eff} for BOUS and QG. For small Re_{eff} values (at coarser resolutions), dissipation takes place at scales that are only slightly separated from the forcing on the domain scale and the primary instability near L_r. In this regime, both BOUS and QG show a comparable dissipation efficiency. For increasing Re_{eff}, the dissipation scales are smaller and smaller, and a sustained forward energy cascade needs to be established to reach the dissipation scales. In figure 11, we note that QG solutions are increasingly inept at reaching dissipation scales as they move towards smaller and smaller values. In sharp contrast, BOUS is characterized by a forward energy flux that converges towards a constant value for large Re_{eff} values. This result illustrates several important points. First, in the absence of dissipation near boundaries, BOUS is capable of establishing a direct, sustained route towards dissipation. Second, this direct route is essentially non-balanced (non-QG) in nature. QG, although capable of a certain amount of forward energy cascade, is not able to reach the smallest scales in a sustained way. Therefore, once the smaller submesoscale scales are considered and the dissipation is relegated to smaller and smaller scales, QG dynamics are fundamentally insufficient. The fluctuation available potential energy $\mathscr{E}_{af}$ also has a non-zero energy dissipation in BOUS (figure 6). The analogous measure for dissipation efficiency of $\mathscr{E}_{af}$ varies with Re_{eff} in a similar manner to D_{eff} (figure 11).

To study the dependence of the results on Ro, we vary the overall Ro for a fixed Re, although in practice our Ro range is limited by the increasing cost of a BOUS

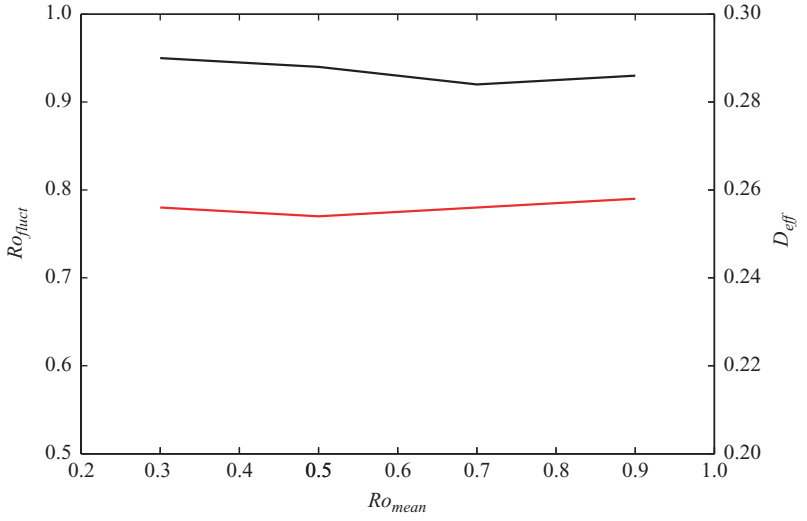

FIGURE 12. Fluctuation Rossby number Ro_{fluct} (measured by the r.m.s. value of the non-dimensional fluctuation vertical vorticity multiplied by Ro; left ordinate and black curve) and dissipation efficiency (right ordinate and red curve) as functions of mean Rossby number $Ro_{mean} = Ro_r$. ($Re_{eff} = 2200$.)

model with decreasing Ro (since the ratio between advection and inertial-wave times increases as Ro^{-1}). In figure 12, the resulting Ro_{fluct} is shown, which is computed by means of the (root mean square) r.m.s. value of the non-dimensional fluctuation vertical vorticity multiplied by Ro. As the figure shows, there is remarkably little variation in Ro_{fluct} for the range of Ro studied. Furthermore, in the spectrum of fluctuation Rossby number (Ro times the Fourier amplitude of the horizontal shear, not shown), there is only a weak dependence on K_h, with values typically around 0.6 at intermediate scales and slowly increasing with wavenumber $\sim K_h^{1/6}$, as expected from the shape of the kinetic energy spectrum $\sim K_h^{-5/3}$ (figure 13). By wavenumber extrapolation, this implies that there should be a finite small scale at which rotational dynamical influences become unimportant; however, we estimate this wavenumber as $O(10^3)$, which is well outside of our model resolution. A similar analysis is made for Fr_{fluct}, defined as Fr times the r.m.s. value of the horizontal gradient of the buoyancy fluctuation (geostrophically proportional to the vertical shear). Note that Fr_{fluct} has a value of about 0.3 on intermediate scales with a similar slow increase in its spectrum with K_h. Thus, $Ro_{fluct} \neq Fr_{fluct}$, which differs from the isotropy expected for geostrophic turbulence for the fluctuations on scales small compared with the domain size (Charney 1971). Furthermore, $Ro_{fluct} > Fr_{fluct}$ is consistent with the submesoscale frontal instability being dominated by horizontal shear and Reynolds stress (§ 5.2). Driven by the energy input by instability of the mean state, the fluctuations develop regions with large gradients in which the local Rossby number becomes $O(1)$. It is in those regions that the forward energy flux towards dissipative scales becomes significant. The interplay between regions that are dissipatively efficient and the continuous generation by the mean-flow instability leads to a fluctuation field where the r.m.s. Ro_{eff} remains almost constant for the range of large-scale Ro values considered here. The behaviour as $Ro \to 0$ can only be inferred by extrapolating the nearly level curves in figure 12.

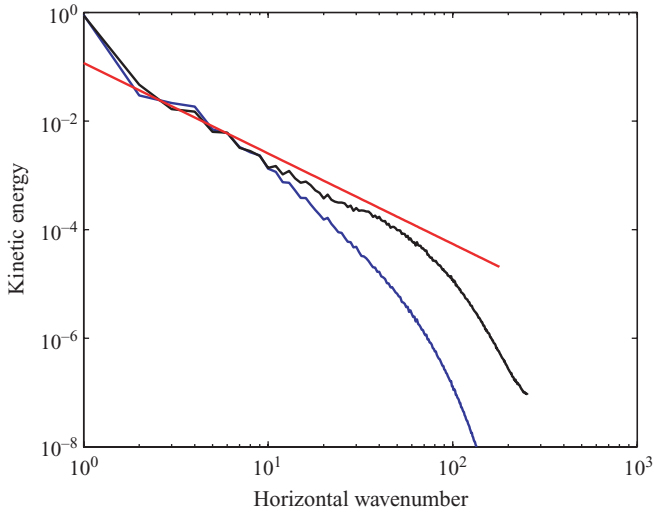

FIGURE 13. Time- and depth-averaged horizontal kinetic energy spectra ($Re_{eff} = 6600$): BOUS ($Ro_r = 0.5$, black) and QG (blue). Spectra are normalized by the mean of kinetic energy $\mathscr{E}_k$. A red line $\propto k^{-5/3}$ is plotted for comparison.

4.3. *Spectral energy balance*

To further examine the flow of energy across horizontal scales, we use a spectral representation of the energy balance. This allows for a more quantitative analysis of forward energy flux and dissipation. Equation (2.7) for $\mathscr{E}_{kf}$ is transformed into an equation for $\hat{E}_{kf}(k_x, k_y, z)$, the fluctuation kinetic energy as a function of horizontal wavenumber (k_x, k_y) and z using a two-dimensional Fourier transform:

$$\frac{1}{2}\frac{\partial \hat{\boldsymbol{u}}\cdot\hat{\boldsymbol{u}}^*}{\partial t} = -\hat{\boldsymbol{u}}\cdot\widehat{(\boldsymbol{u}\cdot\nabla)\boldsymbol{u}}^* + \hat{\boldsymbol{u}}\cdot\widehat{\nabla p}^* + \hat{w}\cdot\hat{b}^* + \hat{\boldsymbol{u}}\cdot\widehat{\boldsymbol{D}}^*. \tag{4.2}$$

Here, $\hat{s}(k_x, k_y, z)$ indicates the complex spectral amplitude. For this analysis, the advection term $(\boldsymbol{u}\cdot\nabla)\boldsymbol{u}$ is computed using a strictly non-dissipative, centred advection scheme. By recomputing the same advection term using the QUICK advection scheme used in the model and taking the difference, we can compute the numerical dissipation present in the model. This numerical dissipation is added to the explicitly computed dissipation of the form $\boldsymbol{u}\cdot\nabla^2\boldsymbol{u}$, shown in (4.2) as the final term on the right-hand side. The second term on the right-hand side represents the work done by pressure. For our domain configuration (horizontally periodic with closed top and bottom boundaries), this term is identically zero for every (k_x, k_y) wavenumber when vertically integrated over the full domain. The third right-hand side term is the release of potential energy by vertical motions.

The spectra are vertically domain-integrated and time-averaged and are plotted as a function of horizontal wavenumber magnitude, $k_h = \sqrt{k_x^2 + k_y^2}$. Both BOUS and QG spectra for E_{kf} have a peak at large scales, where they are quite similar (figure 13). The BOUS spectrum decreases more shallowly with k_h than QG, indicating greater submesoscale energy, and it approaches the $\sim k_h^{-5/3}$ shape of an anisotropic kinetic-energy inertial range at large k_h (consistent with the forward cascade in figure 15). For smaller wavenumbers, the spectral slope of E_{kf} is very similar for both BOUS and QG. For higher wavenumbers, the energy spectrum for QG falls off faster than the BOUS

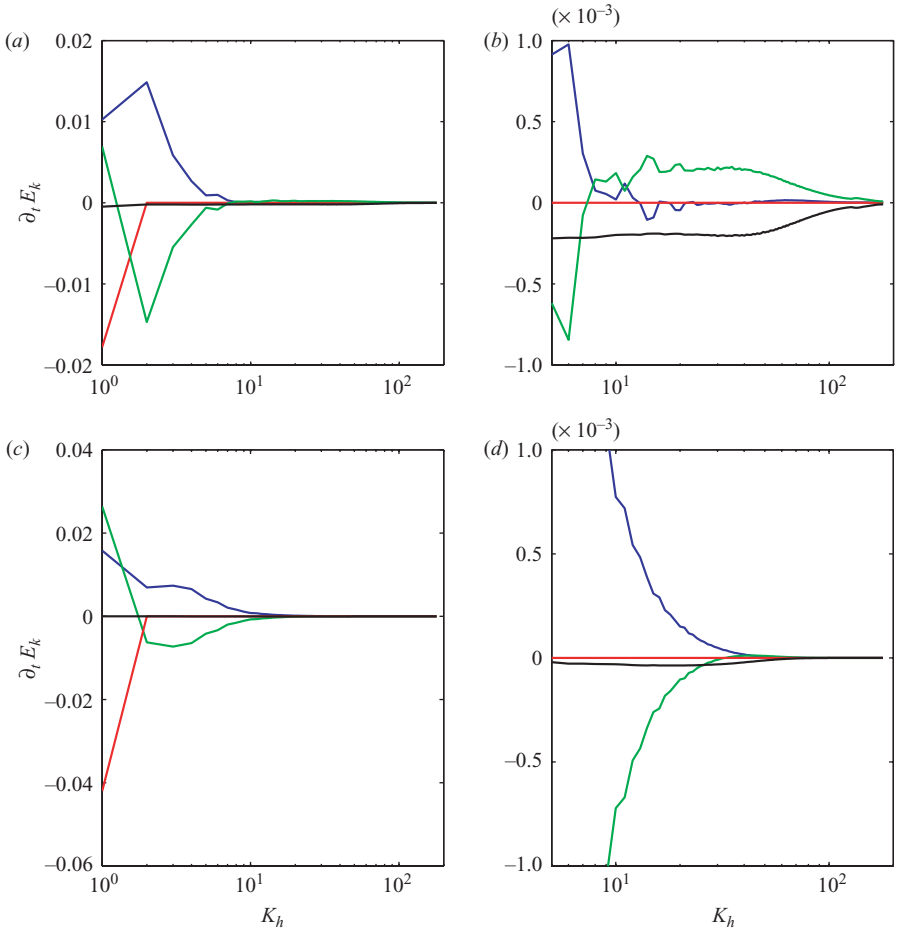

FIGURE 14. Kinetic energy balance in spectral space ($Re_{eff} = 2200$): BOUS ($Ro_r = 0.5$, *a,b*) and QG (*c,d*). Terms are conversion of potential energy (blue), advective flux divergence (green), restoring damping of wavenumber 1 (red) and dissipation (black). Panels (*b,d*) have an expanded ordinate for the higher wavenumbers.

spectrum, and at $k_h = 100$ there are two orders of magnitude difference in kinetic energy between the models. These differences in E_{kf} at higher wavenumbers reflect the differences in dissipation efficiency. Note that these spectra are volume-integrated quantities, as appropriate for the whole-system energy conservation principle. The surface kinetic energy spectrum in the QG model solution is much shallower and does approach a $k^{-5/3}$ slope as predicted for a SQG model of Blumen (1978) and as demonstrated by Capet *et al.* (2008*a*) and Tulloch & Smith (2009); this spectral regime is associated with an inverse E_{kf} cascade and a forward E_{af} cascade.

The individual terms in the spectral energy balance (4.2) are plotted in figure 14. The co-spectra are vertically integrated and averaged in time. The sum of these terms was compared to the accumulated change of kinetic energy $\hat{E}_{kf} = 1/2\hat{\boldsymbol{u}}\cdot\hat{\boldsymbol{u}}$ during the averaging period to verify correctness of the balance and to verify that the time-averaged trend in $\hat{E}_{kf}(k_h)$ is small compared to individual terms in the balance. Figures 14(*a*) and 14(*b*) show the BOUS results, and figures 14(*c*) and 14(*d*) show QG results. In red, the effect of the damping at $k_h = 1$ is shown. As expected, the

damping provides a sink for E_{kf}, acting exclusively at $k_h = 1$. The blue line is the release of potential energy, and it has a peak at $k_h = 2$ for BOUS and $k_h = 3$ for QG, corresponding to the most unstable baroclinically unstable mode of the basic states. QG has an even stronger peak at $k_h = 1$. This results from the fact that there is a very large amount of energy in the $k_h = 1$ spectral component. Even though that mode is less effective in releasing potential energy than the most unstable mode at slightly higher wavenumbers, it still releases more potential energy in an absolute sense. The green line is the effect of the momentum–advection term. When integrated over the wavenumber range, this term is identically zero, so it provides only a redistribution of energy across wavenumbers. With this information we can interpret the balance of E_{kf} at $k_h = 1$. Both BOUS and QG release potential energy at that wavenumber, and in addition both solutions show an inverse energy cascade: energy is transferred from higher wavenumbers by means of the advective term. These two sources of energy are balanced by the large-scale damping. Figure 14(*b,d*) displays the spectral energy balance for an expanded wavenumber ordinate at large k_h. The diffusive term is visibly non-zero for BOUS. BOUS shows that release of potential energy becomes negligible for $K_h > 20$, where dissipation balances the energy that is forward transferred by the advective terms. QG provides a very different picture for energy equilibration: the release of potential energy at relatively small wavenumbers is balanced by an inverse energy cascade, and the small-scale dissipation remains very small.

An examination of the spectra of the terms in the vertical momentum equation shows that the gravitational force $\hat{\boldsymbol{z}}b$ contributes significantly to the fluctuation dynamical balance throughout the energy inertial range up to the onset of the dissipation range. This indicates that the advective forward cascades in kinetic energy and APE are dynamically coupled with each other. This is consistent with a small non-dimensional Ozmidov scale of the flow $L_{oz} = \sqrt{D_{kf}/(\partial_z \mathscr{B})^{3/2}}$ where three-dimensional overturning motions become energetically possible. Its value is about 0.05 for the runs with large Re values. Since the horizontal grid spacing of the runs at the highest resolution is $\Delta x \approx 0.02$, we therefore are not resolving the expected small-scale transition from anisotropic rotating, stratified turbulence to isotropic turbulence when the buoyancy stratification and APE become dynamically irrelevant; i.e. our anisotropic diffusivities are dissipating the energy on small scales in the solutions before such a transition. However, by extrapolation of the forward energy cascade in our solutions, we can anticipate that such a transition would occur on smaller scales if they were better resolved. The discussion around figure 12 further confirms the significant influences of rotation and stable stratification on all of the well-resolved scales in our solutions.

The energy cascade can be expressed explicitly in terms of a spectral kinetic energy flux Π defined by

$$\Pi(k_h) = -\int_{k=0}^{k=k_h} \hat{\boldsymbol{u}} \cdot \widehat{(\boldsymbol{u} \cdot \nabla)\boldsymbol{u}}^{*} \, \mathrm{d}k. \tag{4.3}$$

Since advection is purely a redistribution term over wavenumbers, its wavenumber-integrated effect must be zero when computed correctly; hence $\Pi(0) = \Pi(k_{max}) = 0$. Both BOUS and QG $\Pi(k_h)$ curves show a negative (inverse) energy flux for small wavenumbers (figure 15). For higher wavenumbers ($k_h > 3$) the results significantly differ: BOUS has a consistent forward energy flux, nearly constant for a range up to $k_h = 20$ (as in a kinetic energy inertial range), whereas QG has a negative energy flux (inverse cascade) for all wavenumbers. These curves are consistent with earlier remarks that QG is incapable of reaching dissipation scales at large Re_{eff}. In

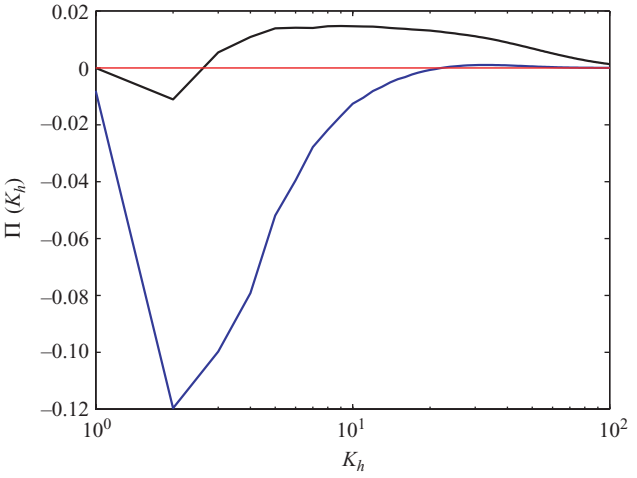

FIGURE 15. Spectral flux of kinetic energy ($Re_{eff} = 6600$): BOUS ($Ro_r = 0.5$, black) and QG (blue). Note the forward cascade for BOUS and inverse cascade for QG.

contrast, BOUS is characterized by a sustained forward energy cascade, allowing for a dissipation efficiency that becomes independent of the Re value for large Re.

Our results for the QG energy cascade are consistent with, and partly anticipated by, the closure-theoretic analysis by Hoyer & Sadourny (1982) of randomly forced, equilibrium turbulence in a two-boundary, quasigeostrophic flow with zero interior potential vorticity. They show that a large-scale, baroclinic, fluctuation energy source (analogous to fluctuation generation by instability of the Eady flow in our problem) has a volumetric total energy cascade that is net inverse, but with a finite wavenumber range of forward volume available potential energy cascade with $wb' > 0$ conversion to volume kinetic energy; the total energy forward cascade asymptotically vanishes as $k \to \infty$ when $Re \to \infty$ (their figures 2 and 5). Note that our results do not contradict the well-established notion that available potential energy at the top and bottom boundaries has a sustained forward cascade towards small scales (Blumen 1978; Hoyer & Sadourny 1982). However, even though it may be tempting to focus on surface quantities only for QG (because for zero interior potential vorticity, all dynamics are controlled by advection of temperature at the boundaries), there is an implied flow in the interior, and the physically relevant energy measure remains a volume-averaged quantity.

5. Unbalanced flow

A central issue is the degree to which the BOUS flow satisfies a diagnostic force balance. The more general horizontal force balance is gradient-wind balance, where Coriolis force, pressure-gradient force and the advective centrifugal force in curved flows provide the dominant terms in the divergence of the horizontal momentum equation (McWilliams 1985):

$$-\nabla \cdot (\boldsymbol{u}_h \cdot \nabla_h \boldsymbol{u}_h) + f\zeta^z = \frac{1}{\rho}\nabla_h^2 p. \tag{5.1}$$

We assess the degree of balance in our solutions as the departure from (5.1) suitably normalized to provide a relative measure:

$$\varepsilon_{gw}(\mathbf{x}, t) = \frac{\left|\nabla\cdot(\boldsymbol{u}_h\cdot\nabla_h\boldsymbol{u}_h) - f\zeta^z + \frac{1}{\rho}\nabla_h^2 p\right|}{|\nabla\cdot(\boldsymbol{u}_h\cdot\nabla_h\boldsymbol{u}_h)| + f|\zeta^z| + |\frac{1}{\rho}\nabla_h^2 p| + \mu}. \tag{5.2}$$

Note that $\mu = f\zeta^z_{rms} + |(1/\rho)(\nabla_h^2 p)_{rms}$ is added to the denominator to exclude situations with locally weak force divergences from being identified as significantly unbalanced. The degree of unbalance thus lies between $\epsilon \approx 0$ (highly balanced or weak) and $\epsilon \approx 1$ (fully unbalanced). An alternative, less restrictive, measure of unbalance based on geostrophic balance is

$$\varepsilon_{geo}(\mathbf{x}, t) = \frac{\left|f\zeta^z - \frac{1}{\rho}\nabla_h^2 p\right|}{f|\zeta^z| + |\frac{1}{\rho}\nabla_h^2 p| + \mu}, \tag{5.3}$$

but this fails to recognize strong vortices as balanced by excluding the centrifugal force divergence included in (5.2). An analogous measure to assess the degree to which the solutions are in hydrostatic balance is

$$\varepsilon_{hydro}(\mathbf{x}, t) = \frac{|-\partial_z p + b|}{|\partial^z p| + |b| + \mu}. \tag{5.4}$$

For (5.4), $\mu = (\partial^z p)_{rms} + b_{rms}$ is added to the denominator.

Note that ε_{gw} and ε_{hydro} for the BOUS solutions indicate that the flow, in most places, is highly balanced. This is seen in figure 16, which is a snapshot of a local region around a stable front. Outside the frontal region, the solution is nearly in both gradient-wind balance and hydrostatic balance. However, at the front, large unbalance is evident. This unbalance is consistent with an inherently unbalanced secondary circulation around a front that is undergoing active frontogenesis (Hoskins & Bretherton 1972). A buoyancy gradient that is being strengthened through the influence of a larger-scale straining field undergoes geostrophic adjustment by means of a restratifying secondary flow, comprised of upwelling (downwelling) on the more (less) buoyant side of the front. This circulation is clearly evident in figure 16 in vertical velocity w with significant unbalance in ε_{gw}. In general, the flow is almost perfectly in hydrostatic balance except for a small part of the front.

Figure 17 is an analogous depiction for another frontal region that is actively unstable as evidenced by the abundance of small-scale features. This instability limits the degree to which the front may be further sharpened by a larger-scale straining field. This small-scale frontal instability enhances both vertical and horizontal mixing (§ 5.2). The small-scale motions exhibit significant gradient-wind and hydrostatic unbalance.

During spin-down (§ 3), the solutions have similar spatial patterns and degrees of unbalance. In the late stages of spin-down (e.g. figure 2), the solutions are in nearly perfect gradient-wind and hydrostatic balance. This is a result of a cessation of active generation of new fluctuations and the completed dissipation of all unbalanced motions.

5.1. *Energy cascade*

The comparison between QG and BOUS solutions demonstrates a dramatic difference in the ability to establish a forward cascade route towards dissipation. Although QG turbulence is characterized by an inverse energy cascade (Charney 1971), the BOUS

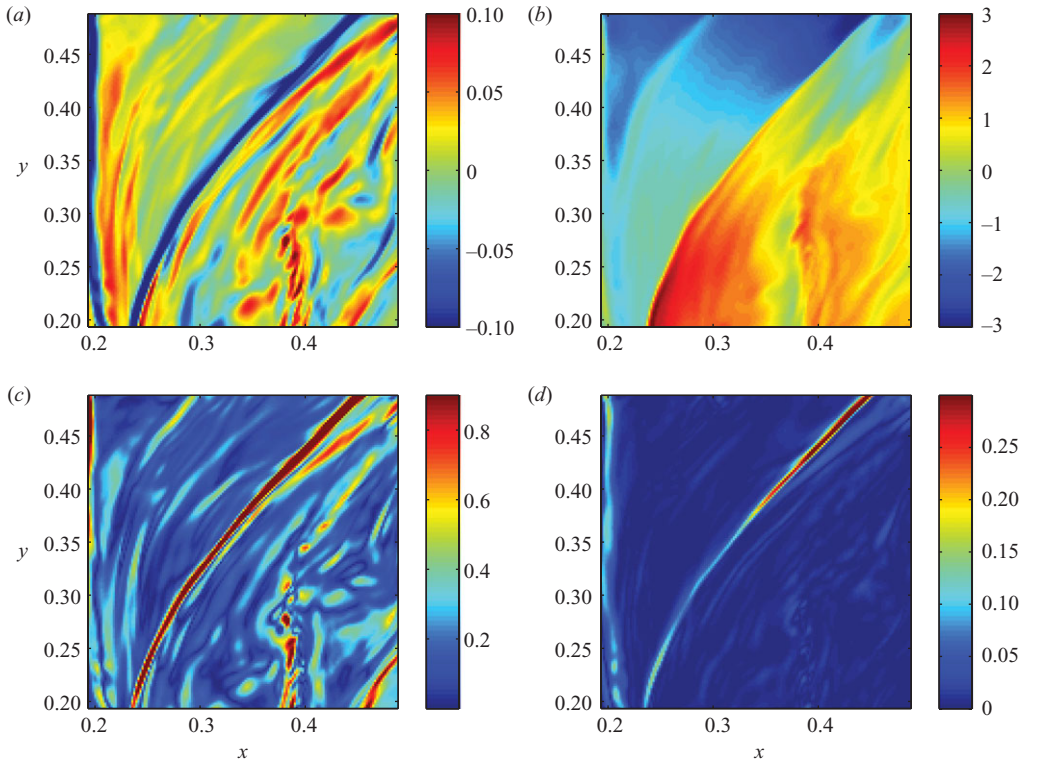

FIGURE 16. A local region with ∼ stable submesoscale frontogenesis in BOUS ($z = 0.96$, $Ro_r = 0.5$, $Re_{eff} = 6600$): (a) vertical velocity, (b) buoyancy, (c) error in gradient wind balance ε_{gw} and (d) error in hydrostatic balance ε_{hydro}.

equations evidently provide for the possibility of a forward cascade. Our experiments show that even when most of the BOUS solutions is in balance—even the simpler geostrophic balance—the flow generates sufficient unbalanced motions to initiate a forward energy cascade.

A formal decomposition of a solution into balanced and unbalanced components is a topic of continuing debate. It is not yet clear whether such a split will have a meaningfully unique answer. However, a simplest approximation for such a split is to orthogonally project the full velocity field of the BOUS solutions $\boldsymbol{u}$ onto a velocity field $\boldsymbol{u}_{nd}$ that is horizontally non-divergent, $\nabla_h \cdot \boldsymbol{u}_{nd} = 0$. This projection matches the property that geostrophic velocity is non-divergent. Figure 18(a) is the kinetic energy spectra for $\boldsymbol{u}$ and $\boldsymbol{u}_{nd}$. As expected, for smaller wavenumbers, the energies in $\boldsymbol{u}$ and $\boldsymbol{u}_{nd}$ are indistinguishable, whereas for larger wavenumbers the energy in the unbalanced field may be as much as 50 % of the total energy spectrum, i.e. an approximate equipartition between balanced and unbalanced parts of the flow. The wavenumber-integrated energy contained in the unbalanced flow is only about 2 % of the total.

The energy flux across wavenumbers Π (§4.3) is shown in Figure 18(b), both for the full BOUS solution (as in figure 14) and for the momentum advection associated only with $\boldsymbol{u}_{nd}$ (approximating the flux associated with the balanced part of the flow). It is clear that the forward energy cascade depends on the unbalanced flow in an essential way. The balanced flow leads to a flux Π that is almost completely inverted, sending energy towards larger scales, identical to the QG solutions. This demonstrates

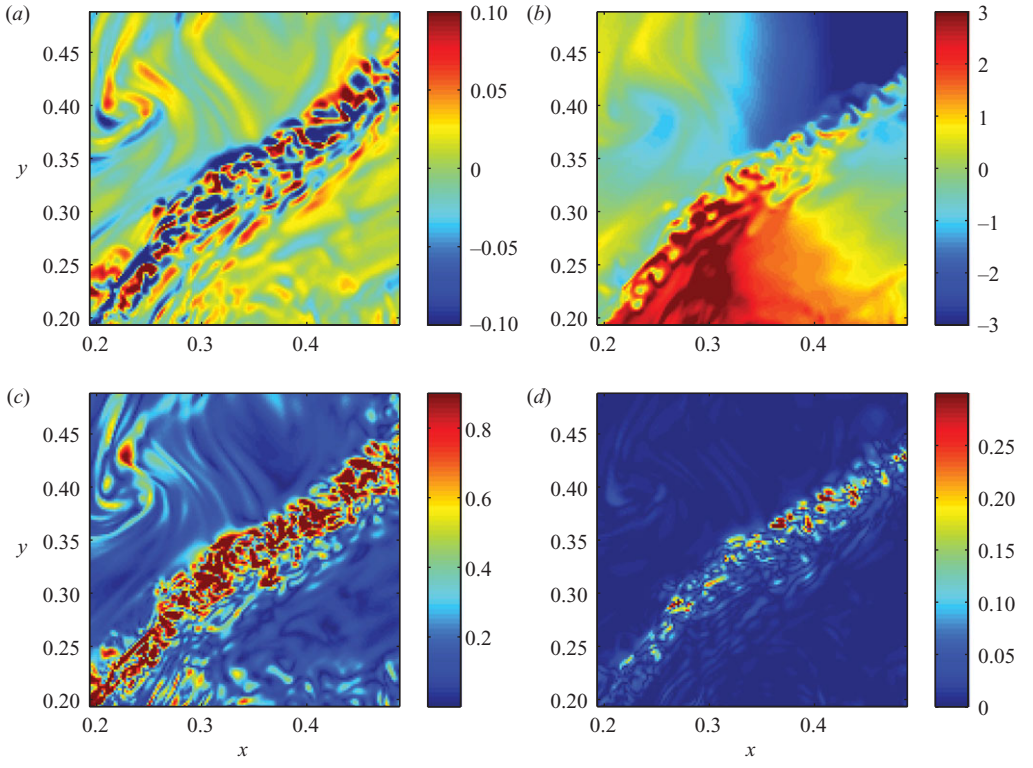

FIGURE 17. A local region with submesoscale frontal instability in BOUS ($z = 0.96$, $Ro_r = 0.5$, $Re_{eff} = 6600$). The format is the same as in figure 16.

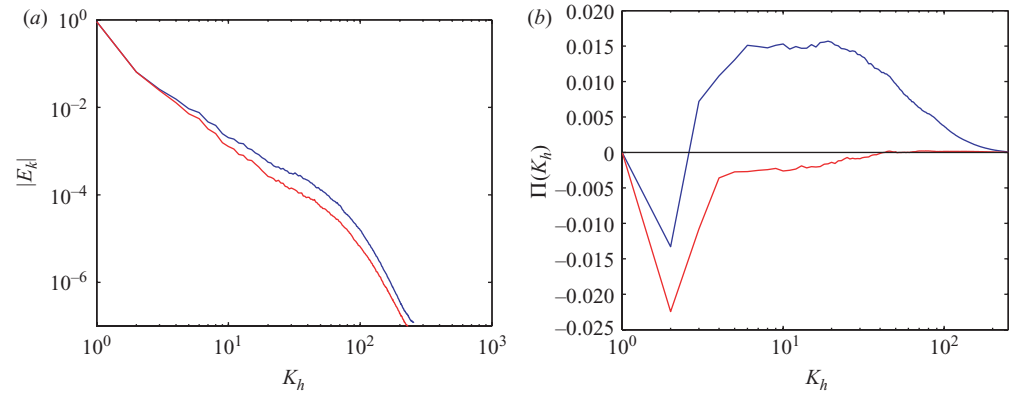

FIGURE 18. (*a*) Three-dimensional kinetic energy spectrum of $\boldsymbol{u}$ for the BOUS solution (blue) and its horizontally non-divergent counterpart $\boldsymbol{u}_{nd}$ (red). (*b*) Spectral flux of kinetic energy for BOUS velocity (blue) and a projected horizontal velocity with $\nabla_h \cdot \boldsymbol{u}_h = 0$ (red). ($Ro_r = 0.5$; $Re_{eff} = 6600$.)

that even when a flow is mostly balanced, as here and in oceanic mesoscale flows, the unbalanced motions may only represent a small fraction of the flow energy, but the motions still have a crucial role in establishing a forward kinetic energy cascade to reach smaller scales where dissipation occurs.

A recent study of subtropical eastern boundary currents also finds a forward kinetic energy cascade in the submesoscale wavenumber range (Capet *et al.* 2008*c*). However, in that study the size of the advection term relative to the energy released by potential energy at high wavenumbers is relatively small, whereas the Eady flow has a much more developed forward cascade extending beyond the wavenumbers of significant potential energy conversion. We would expect that the flow regime of Capet *et al.* (2008*c*) would develop a dominant forward cascade for sufficiently high grid resolution.

5.2. *Fine-scale instability*

For the fluctuations in the BOUS solutions, we can clearly identify two distinct instabilities. At the largest scales, fluctuations arise through baroclinic instability of the mean vertical-shear flow, and as they grow they act to limit its strength. Additionally, a small-scale frontal instability arises and limits the ability of the mesoscale strain field to continue to sharpen the front (cf. figures 5 and 17). The latter is likely to play an important role in the forward kinetic energy cascade.

We focus on a quasi-rectilinear, unstable front to investigate the energy balance for the frontal instabilities by computing energy conversion terms for the local fluctuations relative to the parallel frontal flow. For this purpose, we define a locally rotated reference frame with its y_* axis aligned with the front. The local coordinates are x_* and y_* in the cross- and along-front directions with horizontal velocities u_* and v_*. The front is located at $x_* = 0$. Figure 19 depicts an unstable front in these local coordinates. The vertical velocity is generally downward on the less buoyant side of the front, consistent with a secondary frontogenetic circulation. The secondary circulation pattern is also evident in figure 19(*d*) where along-front averaged velocity vectors are overlaid on the averaged buoyancy field. In addition, a pattern of up- and downward velocity is seen in the fluctuations, indicating an unstable frontal mode. The horizontal slice of buoyancy overlaid with horizontal velocity vectors (figure 19*b*) indicates that the strong frontal buoyancy gradient coincides with an accompanying horizontal divergence.

The local mean $\overline{\cdot}$ is defined as the along-front average, and perturbations to the local mean are denoted by $\cdot'$. Figure 20 plots the energy conversion terms for the fluctuation kinetic energy balance: the horizontal Reynolds stress $\overline{(u'_* v'_*)\overline{v_*}_x}$, the vertical Reynolds stress $\overline{(w v'_*)\overline{v_*}_z}$ and the conversion of potential energy $\overline{(W b')}$. In addition, the figure plots the conversion of potential energy by the along-front averaged flow $\overline{w}\mathscr{B}$. From these x_* and z_* profiles, it is clear that the instability arises mostly from the horizontal shear of the frontal flow and to a lesser extent its vertical shear. Most of the energy conversion is near the surface where the velocity shear is largest. Conversion of potential energy is unimportant for the local energy balance, consistent with its disappearance of $\hat{w}\hat{b}*$ at high wavenumbers in figure 14.

Recently, other studies on submesoscale instabilities find that these instabilities arise because of the release of potential energy rather than the horizontal Reynolds stress (i.e. a baroclinic instability; Boccaletti, Ferrari & Fox-Kemper 2007; Capet *et al.* 2008*b*). One difference between those studies and the current one is the absence here of a surface mixed layer with its reduced vertical gradients. Such a layer introduces a separate, much smaller, mixed-layer deformation radius, implying possible baroclinic instability on a smaller horizontal scale (Capet *et al.* 2008*b*). Furthermore, the enhanced vertical mixing in such a surface mixed layer may alter the potential for different types of instabilities. These various influences on submesoscale and frontal instabilities are not yet fully understood. Another relevant study without a surface mixed layer (Klein *et al.* 2008) finds no evidence of a shear-driven frontal

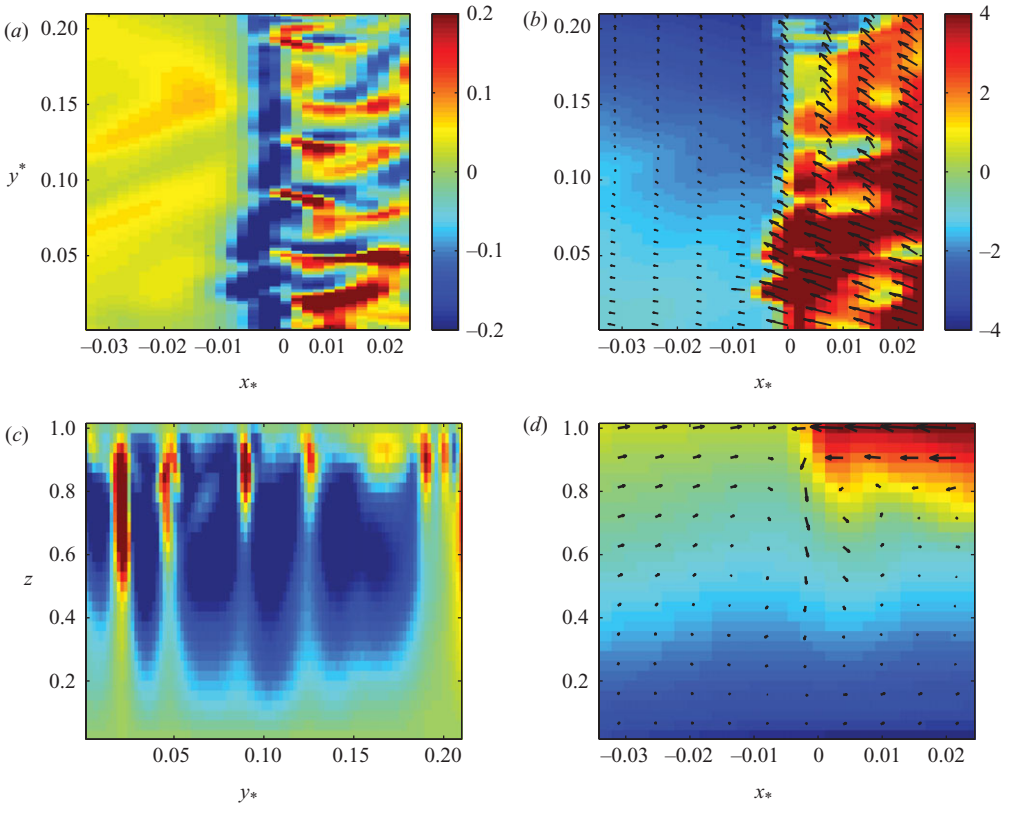

FIGURE 19. A local view of an unstable frontal region. (*a*) Near-surface, horizontal slice for vertical velocity. (*b*) The same for buoyancy with overlaid horizontal velocity vectors. (*c*) Vertical, along-frontal section for vertical velocity at $x_* = 0$. (*d*) Vertical, cross-frontal section of along-front averaged buoyancy and velocity vectors. The local volume-averaged velocity has been subtracted from $\mathbf{v}$ to expose the frontal circulation.

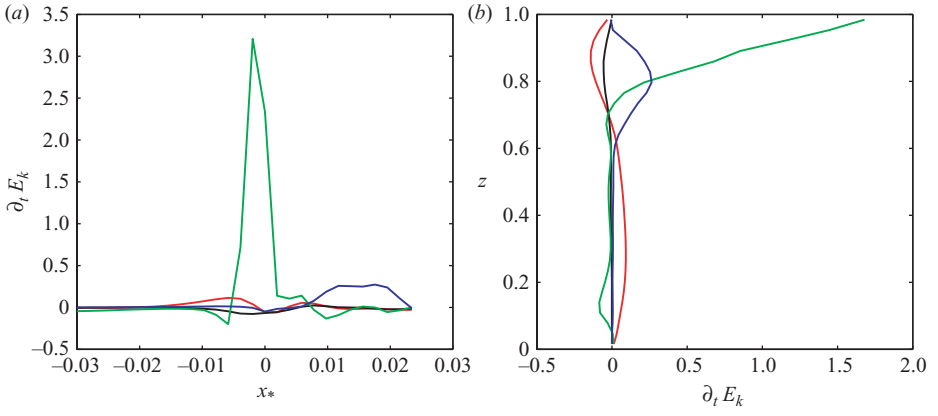

FIGURE 20. Energetics of the frontal instability in figure 19. (*a*) Cross-frontal profiles for depth-averaged kinetic energy production terms and (*b*) vertical profiles averaged over the cross-frontal direction. The production terms are $\overline{(u_*'v_*')}\overline{v_*}_x$ (green), $\overline{(wv_*')}\overline{v_*}_z$ (blue), $\overline{(Wb')}$ (black) and $\overline{w}\mathscr{B}$ (red).

instability. A plausible explanation is that, relative to the first-baroclinic deformation radius, our simulations have finer resolution, allowing the fronts to sharpen further until a horizontal shear instability arises.

6. Summary

We have demonstrated that in the absence of other means of dissipation such as in turbulent boundary layers, a Boussinesq flow is capable of establishing a direct route towards dissipation by means of unbalanced motions and a forward energy cascade. In contrast, a quasigeostrophic flow that by its very nature cannot represent unbalanced motions is markedly incapable of establishing such a direct route and is increasingly non-dissipative for increasing Reynolds number. The Boussinesq flow is energetically dominated by balanced flow, both with regard to gradient-wind balance and even more so to hydrostatic balance. However, the flow develops sharp frontal regions on small scales where locally the fluctuation Rossby number is not small and unbalanced motions emerge. The unbalance in the frontal regions is due to both secondary circulation associated with frontogenesis and frontal instabilities. The frontal instabilities arise primarily from the horizontal shear of the along-front velocity profiles. This means that these unstable modes are neither baroclinic nor convective in their dynamical generation. Unbalanced motions are essential in establishing dissipation by means of a forward energy cascade, as demonstrated by a decomposition of the flow into horizontally non-divergent ($\sim$ balanced) and divergent ($\sim$ unbalanced) components. Although the unbalanced motions represent only a small fraction of the total kinetic energy of the flow, they are essential to the forward energy cascade *en route* to dissipation. As expected from geostrophic turbulence theory, the balanced motions provide an inverse energy cascade towards larger scales and contribute little energy dissipation in the interior region of the flow.

The Eady flow is a special one because of its lack of interior horizontal gradients of potential vorticity (or nearly so with dissipative Boussinesq dynamics); its lack of boundary stresses, buoyancy fluxes and turbulent boundary layers; and its lack of a sharp pycnocline that can isolate some deep interior regions from strong mesoscale or submesoscale currents. It is important that the conclusions we have drawn from the idealized Eady flow be tested in a variety of more realistic flow configurations (e.g. Capet *et al.* 2008*c*).

We appreciate the support of the National Science Foundation through grants OCE 02-21177 and OCE 05-50227.

REFERENCES

Blumen, B. 1978 Uniform potential vorticity flow. Part I. Theory of wave interactions and two-dimensional turbulence. *J. Atmos. Sci.* **35**, 774–783.

Boccaletti, G., Ferrari, R. & Fox-Kemper, B. 2007 Mixed layer instabilities and restratification. *J. Phys. Ocean.* **37**, 2228–2250.

Capet, X., Klein, P., Bach, L.-H., Lapeyre, G. & McWilliams, J. 2008*a* Surface kinetic energy transfer in surface quasi-geostrophic flows. *J. Fluid Mech.* **604**, 165–174.

Capet, X., McWilliams, J. C., Molemaker, M. & Shchepetkin, A. F. 2008*b* Mesoscale to submesoscale transition in the California current system: frontal processes. *J. Phys. Ocean.* **38**, 44–69.

Capet, X., McWilliams, J. C., Molemaker, M. M. J. & Shchepetkin, A. F. 2008*c* Mesoscale to submesoscale transition in the California current system. Part III: energy balance and flux. *J. Phys. Ocean.* **38**, 2256–2269.

Charney, J. 1971 Geostrophic turbulence. *J. Atmos. Sci.* **28**, 1087–1095.

Eady, E. 1949 Long waves and cyclone waves. *Tellus* **1**, 33–52.

Held, I., Pierrehumbert, R., Garner, S. & Swanson, K. 1995 Surface quasi-geostrophic dynamics. *J. Fluid Mech.* **282**, 1–20.

Hoskins, B. & Bretherton, F. 1972 Atmospheric frontogenesis models: mathematical formulation and solution. *J. Atmos. Sci.* **29**, 11–37.

Hoyer, J. & Sadourny, R. 1982 Closure modelling of fully developed baroclinic instability. *J. Atmos. Sci.* **39**, 707–721.

Klein, P., Bach, L., Lapeyre, G., Capet, X., LE Gentil, S. & Sasaki, H. 2008 Upper ocean turbulence from high resolution 3-D simulation. *J. Phys. Ocean.* (in press).

Leonard, B. P. 1979 A stable and accurate convective modelling procedure based on quadratic upstream interpolation. *Comput. Meth. Appl. Mech. Engng* **19**, 59–98.

Lindborg, E. 2005 The effect of rotation on the mesoscale energy cascade in the free atmosphere. *Geophys. Res. Lett.* **19**, 59–98.

Lorenz, E. 1955 Available energy and the maintenance of the general circulation. *Tellus* **7**, 157–167.

McWilliams, J. 1985 A note on a uniformly valid model spanning the regimes of geostrophic and isotropic, stratified turbulence: balanced turbulence. *J. Atmos. Sci.* **42**, 1773–1774.

McWilliams, J. 2003 Diagnostic force balance and its limits. In *Nonlinear Processes in Geophysical Fluid Dynamics* (ed. O. Velasco Fuentes, J. Sheinbaum & J. Ochoa), pp. 287–304. Kluwer.

Molemaker, M. & Dijkstra, H. 2000 Stability of a cold-core eddy in the presence of convection: hydrostatic versus non-hydrostatic modelling. *J. Phys. Ocean.* **30**, 475–494.

Molemaker, M. J. & McWilliams, J. C. 2010 Local balance and cross-scale flux of available potential energy. *J. Fluid Mech.* **645**, 295–314.

Molemaker, M. & Vilá-Guerau de Arellano, J. 1998 Control of chemical reactions by convective turbulence in the boundary layer. *J. Atmos. Sci.* **55**, 568–579.

Molemaker, M., McWilliams, J. & Yavneh, I. 2000 Instability and equilibration of centrifugally stable stratified Taylor–Couette flow. *Phys. Rev. Lett.* **86**, 5270–5273.

Molemaker, M., McWilliams, J. & Yavneh, I. 2005 Baroclinic instability and loss of balance. *J. Phys. Ocean.* **35**, 1505–1517.

Muller, P., McWilliams, J. & Molemaker, M. 2005 Routes to dissipation in the ocean: the 2d/3d turbulence conundrum. In *Marine Turbulence: Theories, Observations and Models* (ed. H. Baumert, J. Simpson & J. Sundermann), pp. 397–405. Cambridge University Press.

Pedlosky, J. 1987 *Geophysical Fluid Dynamics*. Springer.

Press, W., Flannery, B., Teukolsky, S. & Vetterling, W. 1986 *Numerical Recipes*. Cambridge University Press.

Rhines, P. & Young, W. 1982 Homogenization of potential vorticity in planetary gyres. *J. Fluid Mech.* **122**, 347–367.

Shchepetkin, A. & McWilliams, J. 1998 Quasi-monotone advection schemes based on explicit locally adaptive dissipation. *Monthly Weather Rev.* **126**, 1541–1580.

Stone, P. 1966 On non-geostrophic baroclinic instability. *J. Atmos. Sci.* **23**, 390–400.

Stone, P. 1970 On non-geostrophic baroclinic instability. Part II. *J. Atmos. Sci.* **27**, 721–726.

Tulloch, R. & Smith, K. 2009 Quasigeostrophic turbulence with explicit surface dynamics: Application to the atmospheric energy spectrum. *J. Atmos. Sci.* **66**, 450–467.

Waite, M. & Bartello, P. 2006 The transition from geostrophic to stratified turbulence. *J. Fluid Mech.* **568**, 89–108.

Winters, K., Lombard, P., Riley, J. & D'Asaro, E. 1995 Available potential energy and mixing in density-stratified fluids. *J. Fluid Mech.* **289**, 115–128.